# Design and Demonstration of an Ultrafast Terahertz Spectrometer with Femtosecond Polarization-Resolved Detection Capabilities

Benjamin J. Dringoli

Physics Department, McGill University

Montréal, Québec, Canada

August 2019

A thesis submitted to McGill University in partial fulfillment of the requirements of the degree of Master of Science

Supervised by

Dr. David Cooke

© Benjamin J. Dringoli, 2019

# Abstract

Currently, two-dimensional materials and some material surfaces are under intense study due to quantum effects brought upon by their low dimensionality. Experimentally, the "topological" properties of these systems can be modified and probed by electromagnetic interactions. The terahertz (THz) frequency range is well-suited for this task, with many material energy scales in this regime and large low-frequency electric and magnetic fields able to be applied. As the physics in these systems are often linked to the carrier spin and orbital degrees of freedom, different polarizations of light can also be used to both prepare and probe specific states.

By combining the advantages of these two approaches, the instrument built for this thesis is uniquely capable of THz-pump, ultrafast optical polarimetry-probe measurements, or vice versa. The optical polarization is modulated by a Pockels cell, allowing for rapid switching between different polarization orientations and subsequent lock-in detection. Using these capabilities, the instrument can probe sub-cycle interactions with a driving THz pulse or measure spin-selective carrier dynamics.

This thesis will elaborate on the range of experiments now possible, the design and build process of the instrument itself, calibration and sensitivity tests confirming the resolution enabled by the acquisition hardware, as well as future experiments and a case study in a well known optically active material (ZnTe). It is found that this instrument performs similar to traditional THz spectrometers, and demonstrates the necessary sensitivities to measure small time-resolved circular dichroism, birefringence, and Faraday rotation signals. This performance, combined with the wide array of candidates for materials and physics to observe, represents the creation of a new tool to be used for greater understanding in material physics.

# Abrégé

Les matériaux bi-dimensionels et certains types de surfaces font l'objet d'intenses recherches, puisque leur dimentionalité réduite met en valeur des effets quantiques uniques. Les propriétés expérimentales "topologiques" de ces systèmes peuvent être modifiées et mesurées grâce aux interactions électromagnétiques. Le fourchette de fréquences terahertz (THz) est bien adaptée à cette tâche, puisque plusieurs échelles énergétiques appropriées s'y trouvent et que de large champs électromagnétiques de basse fréquence peuvent y être appliqués. Différentes polarisations optiques peuvent être utilisées pour préparer et mesurer des états quantiques spécifiques, puisque la physique de ces systèmes est souvent liée aux spins des transporteurs de charge.

En combinant les avantages de ces deux approches, un instrument de mesure unique, conçu pour cette thèse, est capable de pompe THz, sonde polarimétrique optique ultrarapide, ou vice-versa. La polarisation optique est modulée par une cellule Pockels, permettant de changer rapidement entre les différentes orientations de polarisation. Utilisant ces aptitudes, l'instrument peut sonder des interactions sous-cycles avec un pulse THz moteur, ou mesurer les dynamiques des transporteurs de charge de manière sélective du spin.

Cette these élabore un domaine d'expériences maintenant possible, la conception et la construction de l'instrument lui-même, la calibration et les tests de sensibilité confirmant la résolution rendue possible par le matériel d'acquisition, en plus d'expériences futures et une étude de cas dans un matériau optique actif bien connu (ZnTe). Cet instrument de mesure performe de manière similaire aux spectromètres THz conventionnels, et démontre que la sensibilité necessaire à la mesure dynamique de dichroïsme circulare, de biréfringence, et de rotation de Faraday. Cette performance, combinée à la pléthore de matériaux candidats et de physique à observer, représente la création d'un nouvel outil à être utilisé pour une meilleure compréhension de la physique des matériaux.

# Acknowledgements

I've had the privilege to work with and grow alongside many students, academics, and others that have influenced my path and brought me to the place I am now.

First and foremost, I'd like to thank the entire crew, past and present, of Cooke Lab. Lauren, David, Dom, Yang, and Aidan, without you guys I'd still be lost in a maze of optics without a sense of direction, here's to more fruitful frustration and discovery. Aidan, thanks for your many hours of help in the lab building something from nothing and being there for the occasional heart-to-heart. Above all I'd like to thank Dave for his mentorship and patience in nurturing my curiosity and helping me learn the skills necessary to get to this point. I hope I can dissect and learn about how you stay so energized and focused on understanding the world around you. Special thanks to Laurent René de Cotret for help with the French abstract translation.

Similarly, I'd like to the acknowledge the folks at WPI who helped me make the decision to be here in the first place and to push outside of my comfort zone. Most of all, Lyuba, thanks for your infectious energy, time, and understanding, and for showing me that a love for learning involves collaboration and teaching those around you. As for Taylor, Zach, Peter, and everyone else in the Lounge, the memories of long nights and good laughs keep me going.

Finally, thanks to my family for always supporting me and pushing me to continue to work hard at things I find interesting, I find it a privilege to have this path and such good people supporting me on my journey through it. Mom and Dad, you've given me everything I could have wanted, just keep being there. Liz, we're both grown up but you're still the little voice of reason helping me stay on the straight-and-narrow, and I'm better for it. Sierra, I don't think anything could repay you for the amount of support you've provided these past years and especially the past couple of months, I'm forever grateful.

Here's to learning more throughout this crazy thing we call life.

# Thesis Contributions

- Benjamin Dringoli (BD) and supervisor David Cooke (DC) conceptualized the project and set thesis goals
- BD conducted the literature review and calculated expected responses from previous works
- BD and Cooke Lab PhD student Aidan Schiff-Kearn (ASK) designed and constructed the new beamlines, with guidance from DC
- BD and ASK performed the initial alignment and optimization of the THz spectrometer
- BD performed the Pockels cell system setup, alignment, and regular adjustment
- BD designed and recorded the various calibration datasets
- BD and DC conceptualized the case study, BD took all case study measurements
- BD performed all data analysis procedures for the calibration and case study measurements
- BD wrote all thesis chapters with edits from DC; the French translation of the abstract was provided by Siwick Lab PhD student Laurent René de Cotret

# Contents

# List of Figures

# Chapter 1

# Introduction

Within solid-state physics, there have been many advancements in the past century that have improved our ability to understand and engineer the properties of materials. These milestones, which include the energy band formulation by Bloch [1], the description of electronic properties by Drude [2] and Sommerfeld [3], observation of quantum phenomena such as the quantum Hall effect [4], and more recent discoveries such as the unique properties of graphene [5], have created the framework that now forms the basis for all our computing, sensing, and energy conversion technologies. But as with all innovation, the devices of the future will inevitably need material properties beyond those that exist today. The question then becomes: How does one create and characterize these new properties? Recently, two-dimensional (2D) material systems and material surfaces have become promising candidates for the observation of novel quantum effects and phases [6], which could be used in next-generation devices if understood. As such, new tools to characterize and engineer these new systems will be required; one possible approach involves expanding the capabilities of ultrafast terahertz (THz) spectroscopy.

THz pulses and time-resolved spectroscopy methods using them have become important tools for probing low-energy (1-100 meV scale) carrier dynamics in solid-state systems [7]. Interactions with single cycle THz pulses following optical excitation measure photoconductivity when the field-dependent interactions (dipole, diamagnetic) are small compared to the energy scales of the system and the system is responding linearly to the field [8]. This type of spectroscopy has been applied to study a variety of materials on sub-picosecond time scales after femtosecond (fs) optical excitation [7,9–12]. Furthermore, strong field THz pulses allow one to exceed this limit, entering into the nonlinear response regime where the THz fields (both electric and magnetic) can strongly influence the properties of the material [13, 14]. Many materials studied with these techniques have been spin degenerate, so the polarization

state of the optical pump pulse has no effect on the physics being measured. In 2D systems, symmetry breaking (intrinsic or dynamic) can cause spin-degeneracy to be lifted [15]. This allows for the excitation of carriers with particular spins or which reside in localized parts of the material's energy landscape, depending on the polarization of the excitation pulse. These are important new degrees of freedom for use in next-generation devices, going beyond the usual charge degree of freedom, and defining the fields of spintronics [16] and more recently valleytronics [17], respectively. This selectivity can be combined with ultrafast methods to resolve spin and valley dynamics in materials on fs time scales, which in 2D systems show many promising possibilities for devices as well as interesting fundamental physics.

This thesis describes the design, construction, and characterization of a new instrument that can probe fs spin and orbital dynamics in 2D systems, and can operate in two different overarching modalities. The first is fs polarization-selective pump - THz probe, where the spin and orbital state of the initial charge carrier population in the material is controlled via polarization selection rules [15] and followed by the evolution of its photoconductivity measured via THz pulse transmission. This provides information on spin- or orbital-selective scattering rates [17], which influence the photoconductivity and are critical parameters for the characterization of potential spin- or valley-tronic materials. The second mode in which the instrument can operate is THz pump - fs polarimetric probe, where the material is driven strongly from its equilibrium condition by MV/cm-scale electric fields and T-scale magnetic fields [13]. This naturally breaks the symmetry of the material on a sub-cycle time scale, for example breaking spin degeneracy in materials with strong spin-orbit interactions. Also, strong multi-cycle excitations can induce unique modifications to the band structure through Floquet interactions [18, 19], which can then be probed with fs time resolution. The fs polarization-resolved probe allows for measurement of changes in circular dichroism (CD) [15], linear birefringence (LB) [20], or Kerr rotation (KR) and Faraday rotation (FR) [21] caused by these strong perturbations. While this thesis does not yet fully realize this goal as the methods currently used to generate THz do not provide the field strengths needed for nonlinear driving, we outline the main functionalities of this system inspired by these research possibilities.

With these goals in mind, Chapter 2 further outlines the motivations behind this re-

search direction. First, the principles of THz pulse generation, detection, and spectroscopic techniques are presented, as they form the basis for this instrument and the experiments planned for it. Following this, some of the interesting physics present in two-dimensional systems is reviewed, and an explanation of the new components incorporated into the THz spectrometer to access them is provided. This information is synthesized in Chapter 3, which summarizes the many experimental methods for which this instrument can probe the physics of 2D systems. Then, the specifics of the beamline construction for this instrument are given, along with descriptions of how relevant responses are detected. In Chapter 4, the results of time-resolution, polarization modulation, and sensitivity calibrations are presented, showing the ability of this instrument to resolve relevant experimental signatures with high time resolution. These capabilities are demonstrated by a case study of THz generation and detection in $\langle 110 \rangle$ ZnTe, presented in Chapter 5. Finally, Chapter 6 summarizes the work done for this thesis, and outlines the future improvements necessary to reach full functionality as well as early experimental plans to utilize this new instrument.

# Chapter 2

# Motivation

This chapter introduces the generation and detection of THz pulses and the physics of low dimensionality systems. The sources of their relevant features and how these systems can be modified by THz fields or tailored polarization states will be presented, then the specific technology used to achieve these effects in an experiment will be explained.

## 2.1 Terahertz Light

The THz region is a section of the electromagnetic spectrum generally defined as being between 100's of GHz and 10's of THz [8], but currently has no standard definition [22]; it is situated between the millimeter-wave and mid-IR regions. Until about two decades ago, this region was relatively unexplored due to cycle rates in electronics not being fast enough and optical methods not having the materials or processes required to generate sufficiently low IR frequencies. This led to the region being nicknamed the "Terahertz gap", since it was inaccessible for both technologies [22]. With advancements in high peak power pulsed lasers such as amplified Ti:Sapphire systems [8], the THz region has become an accessible and important regime for many practical and scientific applications. Many large-molecule vibrational modes [23], low energy transitions such as superconducting band gaps [8], exciton resonances [24], and many other processes important for understanding material physics [11,12] occur at THz frequencies.

Today, THz pulses generated from fs laser pulses are largely used to study material properties, although more industrial and public uses are being suggested each year [7]. A THz pulse is a free-space propagating, approximately single-cycle electromagnetic transient with a duration of approx. 1 ps [8]. To achieve its short duration, the pulse consists of frequencies which normally extend from 0.3 to 3 THz depending on the optics employed and generation

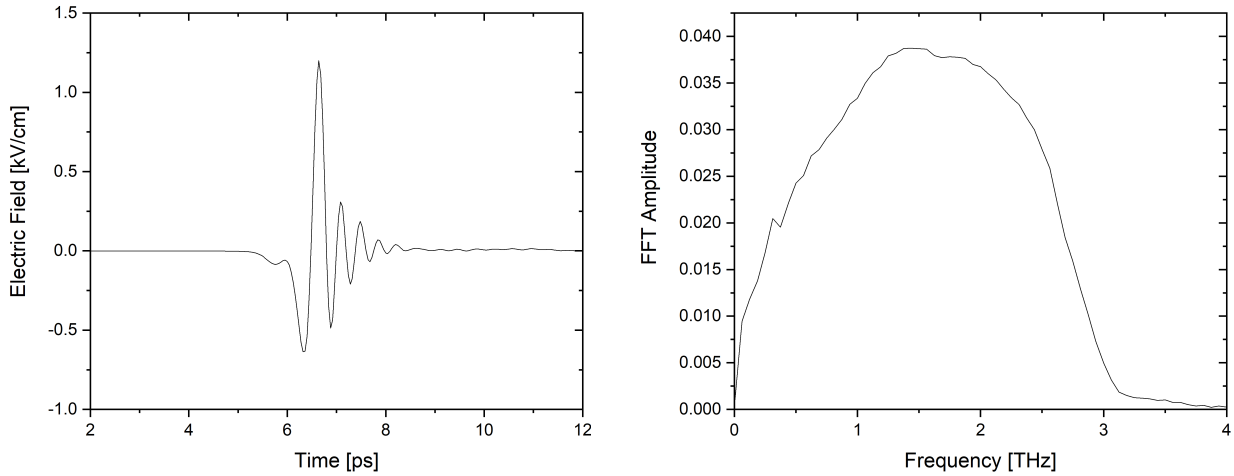


Figure 2.1: A THz pulse generated and detected with ZnTe in this instrument (left) and its corresponding frequency spectrum (right). The THz beam path has been purged with dry air, preventing absorption from atmospheric water vapor [25] and creating a smooth spectrum.

or detection methods (see Sec. 2.2). An example of a THz pulse measured with the instrument built for this thesis is shown in Fig. 2.1. Their short duration and wide frequency range make THz pulses ideal for time-resolved spectroscopy measurements, providing interaction information across a large section of the THz frequency spectrum with sub-ps time resolution.

In addition to the large frequency bandwidth and short duration useful for time-resolved spectroscopy, THz pulses are able to apply large transient electric fields. kV/cm to MV/cm electric fields are possible depending on the generation pulse characteristics and method [13]. With fields this strong, the magnetic field component also becomes appreciable (up to multiple T's). These high fields can strongly perturb material systems, in some cases even pushing responses into the extreme nonlinear regime [14] where the field interaction energy becomes comparable to the energy of a THz photon (1 THz = 4.1 meV). This ability is desirable given that the carrier dynamics in 2D systems can be strongly affected by dressing fields [26, 27]. Strong THz fields also open up possibilities to impart non-negligable momentum onto band carriers, allowing for the k-space dependence of interband transition rules and other physics to be investigated through subsequent optical excitation. Finally, it is possible to narrow the bandwidth of THz pulses to create more periodic-like driving fields, which can be used to dress carriers in 2D systems in novel ways [28]. With these capabilities, THz pulses are extremely versatile as both a transient excitation (pump) and a probe in a frequency range

containing a wealth of material and quasiparticle resonances.

## 2.2 Terahertz Pulse Generation and Detection

### Generation

There have been a variety of techniques used to generate and detect propagating THz radiation since its first demonstration in the late 1980's [9]. These range from accelerating carriers excited from ultrafast pulses to nonlinear conversion methods in optical crystals [7]. For the high energy pulse output of Ti:Sapphire laser systems, nonlinear conversion methods such as optical rectification (OR), shown on the left of Fig. 2.2, are well suited for producing strong THz transients, and are possible in a number of materials [29]. As OR forms the basis for THz generation in this instrument, the theory behind converting ultrafast optical pulses into THz radiation through this process will be presented below.

THz generation in optical crystals is possible through nonlinear optical processes, those for which the electric field $E(t)$ is strong enough to drive carriers beyond a local simple harmonic oscillator-like linear response. This is often due to particular (a)symmetries or arrangements of the material being stimulated: specific differences in atomic lattice structures, electronegativity, or other parameters shape the local atomic potential, creating landscapes away from equilibrium which differ significantly from the harmonic approximation [22]. Since strong driving fields now allow for traversal into these functionally different areas of the potential, the polarization response (related to the shape of the potential) that is normally considered to be static must become field-dependent:

$$P(t) = \chi(E)E(t) = \chi^{(1)}E(t) + \chi^{(2)}E(t)^2 + \chi^{(3)}E(t)^3 + \cdots \tag{2.1}$$

As shown on the right of Eq. 2.1, it is useful to expand the electric susceptibility $\chi$ in powers of $E$, as the effects related to these different terms are distinct and can in many cases be treated separately [30]. Each term can be thought of as a contribution from a different power (quadratic, cubic, quartic, etc.) of a Taylor expansion of the atomic potential, each leading to different kinds of responses to high-field carrier driving.

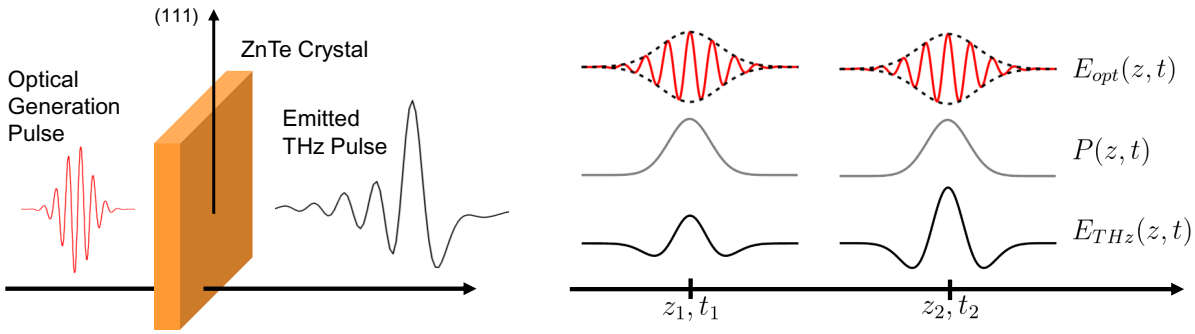


Figure 2.2: Schematic showing the optical rectification process used to generate THz pulses in this instrument. The collinear generation geometry using oriented ZnTe is shown on the left, while the THz amplification process under correct velocity matching throughout the crystal is shown on the right.

OR is a process described by $\chi^{(2)}$, known as a second-order nonlinear process due to its dependence on $E^2$. These processes only occur in non-centrosymmetric media, as they require an asymmetric $x^3$ component in the local potential expansion [22]. This asymmetry causes the electronic motion and subsequent response to differ depending on the drive direction, and dictates the strength of higher-order contributions when acted upon by an AC field. This $E^2$ term leads to two distinct processes when the material is acted upon by a field with multiple frequency components: sum- and difference-frequency generation. OR is a specific instance of the latter.

Considering two frequencies contained in an incident optical pulse $E_1(t) = E_0\cos(\omega_1)$ and $E_2(t) = E_0\cos(\omega_2 t)$, the second order nonlinear polarization is computed as

$$\begin{aligned} P(t) \propto \chi^{(2)} E_1(t) E_2(t) &= E_0^2 \chi^{(2)} \cos(\omega_1 t)\cos(\omega_2 t) \\ &= \frac{E_0^2 \chi^{(2)}}{2} \cos[(\omega_1 + \omega_2)t] + \cos[(\omega_1 - \omega_2)], \end{aligned} \tag{2.2}$$

where the sum and difference frequency components are clear in the final form of Eq. 2.2 [29]. In general all combinations of frequencies present in the input field interact, but the special cases of second harmonic generation and OR occur when $\omega_1 = \omega_2$. By ignoring the $2\omega$ term not important for THz generation, the zero-frequency polarization response due to OR can be described simply by

$$P_0^{(2)} \propto \chi^{(2)} E_0^2. \tag{2.3}$$

As this is a response dependent on the zero frequency component of the applied field, when induced by an optical pulse it follows the Gaussian field envelope $E_0(t) = e^{at^2}$ with the constant $a$ determining the pulse width. By applying Eq. 2.3 with this pulse envelope, a time-dependent nonlinear polarization "pulse" will be induced with a similar functional form: $P(t) = P_0 e^{-2at^2}$ [22].

How this polarization transient produces THz is completely described through manipulation of Maxwell's equations in a medium. The derivation has been explained in many sources [8, 22, 30], and so only the main result will be presented here. The resulting wave equation for the electric field of interest is shown in Eq. 2.4, assuming no free charges are present in the material.

$$\nabla^2 \vec{E} - \epsilon_0 \mu \frac{\partial^2 \vec{E}}{\partial t^2} = \mu \left( \frac{\partial \vec{J}_{free}}{\partial t} + \frac{\partial^2 \vec{P}}{\partial t^2} \right) \tag{2.4}$$

The right-hand side of this equation acts as the source term for the wave equation, and represents the two main ways of generating THz radiation in practice. The first involves inducing and then accelerating free charges with a optical pulse impinging upon a semiconductor under bias, which is the basis for photoconductive switch generation [7]. For OR, the second term is invoked, using the second time derivative of the nonlinear polarization transient explained above as the source for the THz emission. This can be seen in the THz pulse shape in the right of Fig. 2.2. As the polarization transient is comparable in time to the fs optical pulse, the emitted radiation is also extremely fast, usually in the ps range due to a variety of additional effects incurred while travelling through the generation crystal [8].

As the generation crystal is of finite width and the process described above occurs throughout, there are various optical crystal parameters that have a large effect on the efficiency and number of frequencies generated, as well as the THz output's final shape. Since both the optical pulse and therefore the polarization transient propagate through the generation crystal at the optical group velocity $v_{opt} = c/n_{opt}$, if the speed of the emitted THz pulse $v_{THz} = c/n_{THz}$ differs significantly it can stray from its generation pulse when propagating through the material [22]. This spatial decoupling prevents constructive amplification of the THz pulse throughout the generation crystal, and has led to much study of the so-called

phase matching, shown by Eq. 2.5, in nonlinear crystals with large $\chi^{(2)}$.

$$\Delta k(\omega_{THz}) = \frac{\omega_{THz}}{c}[n_{opt} - n_{THz}(\omega_{THz})] \tag{2.5}$$

Improvements in generation efficiency and bandwidth can thus be made either by reducing the velocity (index) mismatch, limiting low-frequency dispersion, or fabricating thinner crystals such that the mismatch has minimal effect. Another figure of merit related to these is the coherence length, calculated as $l_c(\omega_{THz}) = \pi/\Delta k(\omega_{THz})$, which describes the maximum tolerable thickness for a given velocity mismatch [29]. The case of perfect velocity matching is shown on the right of Fig. 2.2. When the THz is propagating at the same speed as the optical and polarization transients, the generated THz is reinforced and amplified throughout the nonlinear crystal until it is emitted. A number of crystals have been found to have phase matching characteristics suitable for THz generation via OR, such as ZnTe, $LiNbO_3$, and GaP, but $\langle 110 \rangle$ ZnTe is currently used for this instrument. As the various generation parameters presented above are optimized for a particular crystal orientation, the rotation angle will also greatly affect the generation efficiency; this is explored in the case study of ZnTe (Chapter 5).

$\langle 110 \rangle$ ZnTe is a popular choice for THz generation using OR due to its collinear phase matching in the near-IR, a frequency range well suited for using the output of Ti:Sapphire amplified laser systems. Taking into account both THz and optical dispersion, it is predicted that the emitted THz will stay coherent with an 800 nm generation pule from approx. 0-3 THz for crystals $< 1$ mm thick [31]. This is confirmed in the 0.5 mm ZnTe crystals used for THz generation and detection in this system, with measured THz frequencies extending until the coherence cutoff around 3 THz, shown in Fig. 2.1. For other materials, the difference in velocities may be too great for collinear OR, even for thin crystals. In this case, the geometry of both the incoming optical pulse and the generation crystal itself can be tailored for optimal THz emission. This is the case for $LiNbO_3$, which is desirable for OR due to its large nonlinear optical coefficient [32]. Schemes such as this have allowed for the generation of THz fields in the MV/cm range [13], and how these capabilities can be incorporated into this instrument are discussed in Chapter 6.

## Detection

For use in spectroscopic studies and to characterize the results of the generation process presented above, ultrafast THz pulses must also be reliably detected. Like generation, detection methods use interactions between the THz and an optical fs pulse to measure the time-dependent THz field with sub-ps resolution. There are two similar main pathways which can be taken: driving excited carriers in a photoconductive switch or measuring nonlinear processes induced by the THz radiation [7]. For this instrument, the nonlinear Pockels effect will be used, enabling a detection scheme known as electro-optic sampling (EOS).

The nonlinear processes used to achieve EOS are derived from the same physics as for OR [29], and therefore are also dependent on $\chi^{(2)}$ and require the presence of a non-centrosymmetric medium. While in OR a field-induced polarization gives rise to an emitted field that follows the pulse envelope, in EOS the THz field, effectively static compared to the optical pulse duration, creates a polarization at the optical frequency [30]. This relation is shown in Eq. 2.6.

$$P_i(\omega) = 2\epsilon_0 \sum_{jk} \chi^{(2)}_{ijk}(\omega = \omega + 0) E_j(\omega) E_k(0) \tag{2.6}$$

Here more detailed notation is used to show that the resulting response frequency is the sum of the optical and quasi-DC THz fields. The induced polarization has the effect of changing the refractive index of the detection crystal along a particular axis $n_i$ according to the material's electro-optical tensor $r_{ij}$, which can be related to $\chi^{(2)}$ [29]. When the optical sampling pulse is overlapped in space and time with the perturbing field, the polarization-induced birefringence applies a slight retardance to the components of sampling pulse along the affected axis, creating a small amount of ellipticity in the sampling pulse polarization.

As with the generation process, concerns around pulse duration and phase matching also apply here. These can be explained by considering a convolution of the time-dependent THz field with an effective detector response function $F(\omega, \omega_{THz})$ for the EOS crystal. Fourier transforming this convolution produces an expression for the EO signal, given in Eq. 2.7.

$$E_{EO}(\omega_{THz}) = F(\omega, \omega_{THz}) \times E_{THz}(\omega_{THz}) \tag{2.7}$$

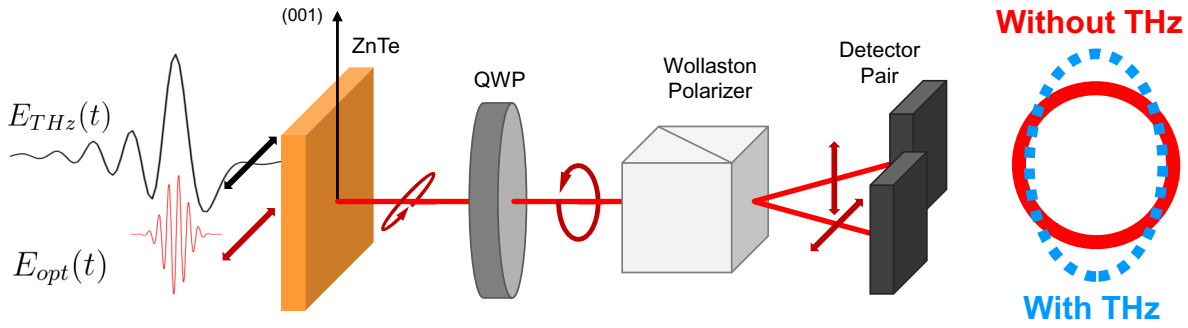


Figure 2.3: Diagram detailing how EOS is used to resolve instantaneous THz fields (left) and the induced change on the sampling pulse (right). The induced birefringence in the ZnTe crystal creates ellipticity in the sampling pulse polarization, unbalancing the linear components after the quarter-wave plate and creating nonzero signal in the differential measurement.

The detector response function contains all of the interaction physics, and in this formulation is a product of three frequency-dependent factors: $\chi^{(2)}$, the optical pulse autocorrelation, and the frequency filtering due to velocity mismatch [22]. The full forms of the latter two are given in Eqs. 2.8 and 2.9.

$$A(\omega_{THz}) = \int_{-\infty}^{\infty} E^*_{opt}(\omega' - \omega) E_{opt}(\omega' - \omega - \omega_{THz}) d\omega' \tag{2.8}$$

$$\Delta\Phi(\omega, \omega_{THz}) = \frac{e^{i\Delta k(\omega,\omega_{THz})L} - 1}{i\Delta k(\omega, \omega_{THz})} \tag{2.9}$$

$A(\omega_{THz})$ takes into account the finite duration of the optical sampling pulse, which limits the detection resolution of the instantaneous THz field, and $\Delta\Phi(\omega, \omega_{THz})$ expresses the effective overlap of constituent frequencies as the two pulses travel together through a crystal of thickness $L$. This overlap has effects similar to the phase matching concerns for THz generation. Calculated values of $F(\omega, \omega_T Hz)$ in various thicknesses of ZnTe are shown in Fig. 3.45 of ref. [22], and show a similar roll-off around 3 THz for the 0.5 mm thickness due to phase matching.

To resolve the small polarization change of the sampling pulse induced by the THz field, a quarter-wave plate (QWP) and polarizing beamsplitter (typically a Wollaston Prism) are placed after the detection crystal, with both outputs from the polarizer sent to individual

photodiodes (PDs). A simplified diagram is shown in Fig. 2.3. In the absence of a THz field, the unaffected linear sampling pulse is converted to circular polarization by the QWP, whose equal linear components are split by the polarizer. When looking at the difference between the PD signals, this produces a null measurement without the presence of a THz field. When ellipticity is induced in the sampling pulse due to the small birefringence from the THz field, the small helical component added onto the main linear polarization is turned into linear polarization by the QWP, and thus creates an imbalance between the normally balanced photodiodes (as the main linear portion is still split into equal orthogonal linear components). This imbalance is linearly proportional to the instantaneous THz field [20, 22], as shown in Eq. 2.10, for the small phase retardations present in EOS setups:

$$\Delta I = I_{tot} \frac{\omega n^3 E_{THz} r_{41} L}{2c} \tag{2.10}$$

Here $\Delta I$ is the differential intensity, $I_{tot}$ is the full sampling beam intensity, $\omega$ is the sampling pulse angular frequency, $n$ is the optical refractive index, $E_{THz}$ is the instantaneous THz field, $r_{41}$ is the appropriate component of the electro-optic tensor, and $L$ is the length of the crystal. This equation can also be used, knowing the incident intensities or voltages from the PDs, to calculate the generated THz field. PD voltages measured for the peak of the THz pulse shown in Fig. 2.1 are used with the crystal thickness $L = 0.5\,\text{mm}$ and ZnTe parameters $r_{41} = 3.9\,\text{pm}\,\text{V}^{-1}$, $n(800\text{ nm}) = 2.8$ from ref. [20] to calibrate the measured THz field, as shown below.

$$E_{THz} = \frac{\Delta I}{I_{tot}} \frac{2c}{\omega n^3 r_{41} L} = 1.27\,\text{kV}\,\text{cm}^{-1}$$

This relatively low peak field is expected for ZnTe generation with limited laser power available, and will soon be upgraded to a more intense $LiNbO_3$ source (see Ch. 6). Both the time- and frequency-domain traces are similar to those shown for THz detection in 0.5 mm-thick ZnTe in Fig. 3.46 of ref. [22], showing that this theoretical treatment accurately describes the THz generation and detection processes in this instrument.

Therefore, by monitoring the differential signal from the two PDs in the balanced detection arrangement, the THz electric field can be resolved. By delaying the faster sampling pulse with respect to the THz pulse, the entire structure of the electric field transient can be

mapped out. The resolution of this mapping is limited by both the step size of the delay stage being used and the duration of the optical sampling pulse, both of which will be addressed in Chapters 3 and 4 when speaking about the beamline design and pulse optimization, respectively. This ability to resolve the field $E$ and not the intensity $I$ allows for full amplitude and phase information to be recorded, the benefits of which will be explained in Sec. 3.1.

## 2.3 Topological Materials

The main goal of this specialized instrument is to use THz methods to investigate new physics and explore possibilities for optical control in topological materials. Here "topological" refers to any system whose properties are directly dependent on its dimensionality [16]. 2D materials such as graphene fall into this category due to their monolayer nature [33], but so do some bulk materials whose surfaces demonstrate starkly different properties from their bulk. This type of effect is most easily explained by considering topological insulators, which are generally insultaing but house conducting states on their surfaces. These conducting states come from the differing "topological invariants" in the bulk material and its surroundings, which one can think of as different loopings or knottings of the electronic wavefunction [16]. Just as the topology of a sphere cannot be transformed into that of a torus without breaking the surface, one cannot pass from on of these insulating knotted states to the other without breaking the loop, which represents the creation of a conducting state at the surface. This and other symmetry- and topology-dependent physics are what currently make these materials so interesting, and optical methods of perturbing these systems or breaking symmetry are well suited for their study, motivated below.

Surface states and two-dimensional materials can be of interest for other reasons as well: in a class of materials known as transition metal dichalcogenides (TMDs), the band structure is significantly modified when the material is thinned down to a monolayer [34]. In many of these materials, this induces a transition from indirect to direct band gap behavior, opening up a variety of possibilities for optical measurement and control. In addition, the strong spin-orbit coupling in these materials [35] causes significant spin-splitting of the bands which differs for different regions of the material's Brillouin zone (BZ) [36]. The spin-dependence of

the transitions allows for specific carrier excitations using circularly polarized photons, which create spin-polarized carrier populations which lie in a particular band valley. This can be measured via differential reflection or transmission of helical light, shown in Eq. 2.11, and denotes what is known as the spin or valley polarization of the excited carriers [15].

$$\frac{\Delta R^{\sigma+} - \Delta R^{\sigma-}}{\Delta R^{\sigma+} + \Delta R^{\sigma-}} = \frac{C_1 - C_2}{C_1 + C_2} \; P \tag{2.11}$$

Here $\sigma+$ and $\sigma-$ represent right- and left-circularly polarized light (RCP and LCP), respectively, $C_{1,2}$ are coefficients describing the absorption properties of spin up and spin down carriers, and $P$ denotes the spin/valley polarization. This polarization and its dynamics is of special interest to those investigating the use of electron spin or location in momentum space for computing or information storage, known as spin- or valley-tronics [6], and can be measured by THz spectroscopy methods. The ability to understand and control these new degrees of freedom has the potential to open up new possibilities for pushing further towards the realization of quantum-based computing.

Circular polarization (CP), sometimes identified as helical polarization, can be a useful tool in exploring these systems as both a tailored perturbation to be probed and a probe for perturbed systems. As the latter, CP light contains additional angular momentum, which permits for more specific transition selection in spin-split systems, as explained above. This allows for experiments performed using the circular polarized pump to have valley- or spin-selectivity, which can then be probed to see its effect on material properties or to elucidate the properties of these particular classes of carries. As the former, circular polarization breaks time-reversal symmetry in the systems it is applied to, which can open band gaps in previously gapless materials such as graphene [37], as well as modify band gaps in already gapped materials. For high-frequency off-resonant excitation in graphene, the gap opened $2\kappa$ by CP light can be described by Eq. 2.12 [38].

$$2\kappa = \sqrt{4\mathcal{A}^2 + \Omega^2} - \Omega \tag{2.12}$$

Here $\mathcal{A} = eaE/\Omega$ is a dimensionless parameter quantifying the interaction with the applied vector potential, $a$ is the lattice constant, and $\Omega$ is the photon energy. At 1 THz with field

strengths from 1-100 kV/cm, this corresponds to a gap of 10-100's of meV [38], resolvable by both THz and optical absorption edge measurements. This induced change could have significant consequences as it represents a path toward ultrafast switching of a material from insulating to conducting, much like a transistor. This interaction is also seen to induce helicity-dependent quantized Hall-like effects without applied magnetic fields [39], opening up another class of experiments for optical methods to probe. Experiments like this will pave the way for the investigation of optical control and novel quantum effects in new materials.

Circular polarization is not the only tool tailored to the interesting properties of these materials. It has been shown in some topological materials that the application of a time-periodic potential can create copies of the allowed band structure in energy space, just as the periodic potential from a crystal lattice forms band copies in momentum space [19]. Computing the modified Hamiltonian for this affected system leads to two statements that can be made about the new energy landscape [40]: (1) if $E(k)$ is a valid despersion relation solution then so is $E(k) + n\hbar\omega$, and (2) that the resulting band structure is symmetric around $k = 0$. Here $n$ is an arbitrary integer, and therefore the new energy band copies are spaced by the dressing photon energy. A diagram of this new band structure is shown in the right panel of Fig. 3.1. These Floquet band copies, named after the time periodic theory used to describe them, can be switched on and off with the application of the pump light, and therefore are well-suited for measurement via time resolved techniques. This effect can also be combined with the gapping effect of circular polarization [19] and band renormalization under applied fields to create a variety of transient energy states which can be studied. Intense THz pulses are strong enough to induce these effects, making THz a valuable tool in working to understand their features and dynamics, whether they be gap opening, band renormalization, or band copying. An extended example of the effects of strong incident radiation on the band properties of these materials is described below.

Following the derivation presented by Kibis et al. [26] for gapped graphene, the interaction with a non-resonant perturbing field can be described by a "dressing" of the electrons, leading to a modified Hamiltonian. This modification of the electron states and band gap is shown to be highly dependent on the polarization of the dressing field. Formulating the full

Hamiltonian of a electron system dressed by linearly polarized radiation gives Eq. 2.13.

$$\hat{\mathcal{H}}(\mathbf{k}) = \begin{pmatrix} 0 & \Omega\tau\hbar\omega/2 \\ \Omega\tau\hbar\omega/2 & 0 \end{pmatrix} \cos(\omega t) + \begin{pmatrix} \Delta_g/2 + \tau s\Delta_{so}^{c}/2 & \gamma(\tau k_x - ik_y) \\ \gamma(\tau k_x + ik_y) & -\Delta_g/2 + \tau s\Delta_{so}^{v}/2 \end{pmatrix} \tag{2.13}$$

In this representation the first term represents the electron-field interaction and the second term is the Hamiltonian of a bare electron. Here $\Omega$ denotes the coupling strength to the electric field, $\tau = \pm 1$ is the spin index, $\omega$ is the angular frequency of the dressing wave, $\Delta_g$ represents the band gap energy, $\Delta_{so}^{c,v}$ gives the spin-orbit splitting, $s$ is the spin index, and $\gamma$ is the electron dispersion parameter. Finding solutions of the nonstationary Schrödinger equation in the high frequency limit for linearly polarized light produces the effective Hamiltonian in Eq. 2.14.

$$\hat{\mathcal{H}}_{eff}(\mathbf{k}) = \begin{pmatrix} \widetilde{\Delta_g}/2 + \tau s\widetilde{\Delta_{so}^{c}}/2 & \tau\widetilde{\gamma_x}k_x - i\widetilde{\gamma_y}k_y \\ \tau\widetilde{\gamma_x}k_x + i\widetilde{\gamma_y}k_y & -\widetilde{\Delta_g}/2 + \tau s\widetilde{\Delta_{so}^{v}}/2 \end{pmatrix}. \tag{2.14}$$

This shows that in this case of a linear dressing field, the effective Hamiltonian is of the same form as that of the bare electron with renormalized band parameters $\widetilde{\Delta_g}$, $\widetilde{\Delta_{so}^{c}}$, and $\widetilde{\gamma_{x,y}}$ [26]. Specifically, the band gap is simply modified by a Bessel function factor dependent on the field coupling: $\widetilde{\Delta_g} = \Delta_g J_0(\Omega)$. Even for modest fields ($< 1$ kV/cm) at THz frequencies, this can lead to changes in the band gap of 50% or more [26]. This band renormalization is also accompanied by a difference in dispersion dependent on the orientation of the perturbing field, which could open up a variety of induced anisotropy studies and have the potential to be monitored by ultrafast optical methods.

The case of circularly polarized dressing adds additional effects due to the different chiralities of the incident light, represented here by $\xi = \pm 1$. Through a similar treatment as the dressing by the linear field, the resulting effective Hamiltonian and electronic states can be calculated. This results in a dressed system where the new effective band gap is shown in Eq. 2.15.

$$\widetilde{\Delta_g} = \tau\xi\hbar\omega + \mathrm{sgn}(\Delta_g - \tau\xi\hbar\omega)\hbar\omega\sqrt{\Omega^2 + \left[\frac{\Delta_g - \tau\xi\hbar\omega}{\hbar\omega}\right]^2} \tag{2.15}$$

This dependence on $\xi$ causes the renormalization to differ between helicities of light as well as between linear and circular perturbations. Most notable is that circular dressing can more

severely shrink or expand the band gap as compared to linearly polarized light of the same incident intensity [26]. This makes the study of these materials and their changes under excitation more accessible with the use of arbitrary polarization capabilities, especially with the ability to resolve the differential response between helicities. Additionally, the gaps in Dirac materials are often on the meV scale, and with these strong modifications they can be expanded by 100-1000%. While this effect is more pronounced, creating strong CP THz pulses to drive these changes is currently difficult. More work will have to be done to see if CP THz pulses can be applied or if the arbitrary polarization states of the optical beam can have an effect on these systems.

The flexibility provided by different available pulse energies, polarizations, field strengths, and pulse durations opens up a multitude of possible research options using ultrafast THz methods in these systems. The novel elements of this instrument's design (circular polarization control and resolution, tailored THz excitation, flexible pump-probe methods) were chosen with these systems in mind, as they can probe and influence the physics as described above. The novel polarization control is accomplished by integrating the particular components explained below.

## 2.4 Polarization Modulation

### Pockels Cell

To achieve the flexible polarization capabilities needed to resolve novel effects in these topological materials, a new device is incorporated in addition to the host of optics and detectors already used in an unmodified THz spectrometer. This device is known as a Pockels cell (PC) and uses the Pockels effect (linear electro-optic effect) to delay certain orientations of incident optical fields by applying high voltages to electro-optic crystals, described by Eq. 2.16 [41]. Combining the cell with an appropriately triggered high voltage, high speed driver allows for pulse-to-pulse polarization switching of the polarization modulation (PM) line in this instrument, shown in Fig. 2.4. This, combined with sensitive lock-in detection, provides

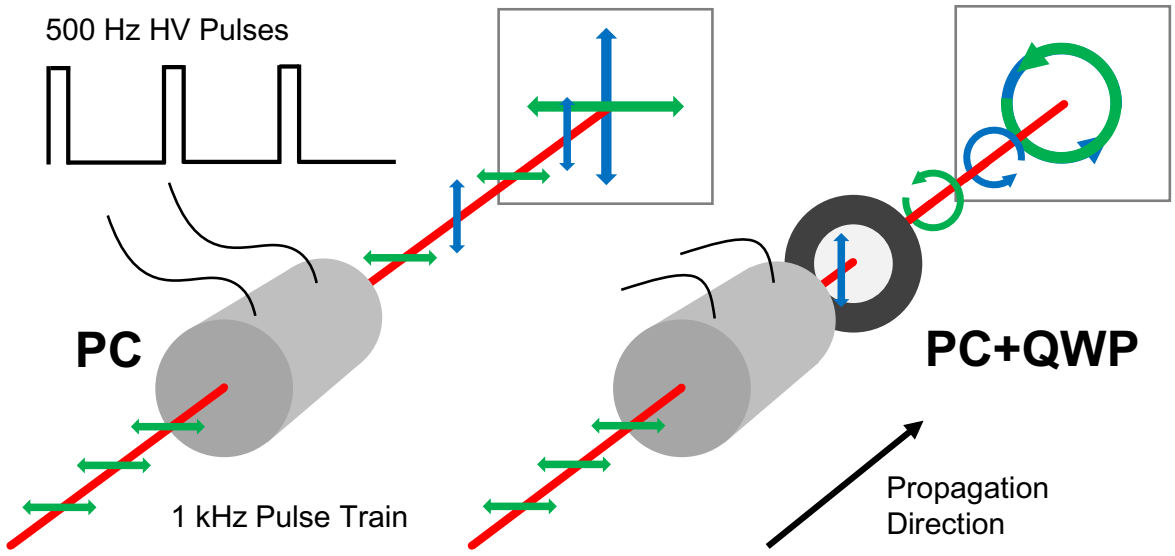


Figure 2.4: Diagram showing pulse-to-pulse polarization flipping using the PC. Both linear (left) and circular (right) modulations are possible with half-wave voltages being applied. This modulation is what allows for the extended use of lock-in detection to measure polarimetry signals.

the sensitivity necessary to perform CD, LB, and FR measurements.

$$\Delta n^{eo} = \frac{1}{2} n^3 r_{ij} V_{app} \tag{2.16}$$

Similar to the electro-optic detection described in Sec. 2.2, the retardance capabilities of the PC come from a change in refractive index along a particular crystal axis induced by an applied electric field. Instead of the smoothly varying THz electric field inducing slight changes in polarization, the PC driver applies rectangular kV pulses to quickly turn the PC into an effective wave plate capable of half-wave retardation. The amount of retardation is controlled by the amount of high voltage (HV) applied, adjustable within a set range determined by the driver used. As the voltage required to achieve a desired amount of retardation is wavelength-dependent, the delay of different frequencies within a high-bandwidth pulse will be slightly different. This affects the ability to perfectly circularly polarize broadband pulses (see Sec. 4.2), but does allow for flexibility if other wavelengths in the near-IR range would be beneficial as probes.

For the capabilities required in this new instrument, the PC can be used without any

additional polarization optics to rotate the incoming linear polarization 90° (half-wave operation) or a QWP can be inserted after the PC to switch from RCP to LCP (or vice versa) while the PC is triggered. This is achieved by orienting the crystal axes at 45° with respect to the incoming pulse linear polarization. This ensures equal intensity along each axis, such that when one is delayed by $\lambda/2$ upon application of the correct HV, the slow axis component effectively reverses polarity. This leads to an orthogonal output polarization with the high voltage applied. Linear modulation is useful for diagnostics as well as measuring LB and linear dichroism, while circular modulation can resolve differences due to the spin and valley indices of excited carriers or directly probe the CD of a material.

The maximum duration that the PC can be in its on state (HV applied) is 3 µs, so the high voltage pulses must be closely synced to the amplifier as the duration of the amplified pulses (approx. 35 fs) is extremely short compared to the time between pulses (1 ms). To accomplish this, a variable delay pulse generator (TTI TGP110) is used to trigger the HV pulses sent from the PC driver. The function generator is itself triggered from the same master clock used to time the entrance and exit of the oscillator pulses into the amplification cavity to ensure correct syncing. The delay of the function generator output is adjusted to compensate for the time difference between signal propagation in coaxial cables and the beam path across the table.

Since these devices are more common in fully-built systems such as amplifier cavities, this standalone device had to be tested and characterized before use in the THz setup. To do this, a simplified beam line was constructed, consisting of an input polarizer, the PC, and a crossed analyzing polarizer, among some other passive optics to control intensity and/or bandwidth. Each output of the analyzing polarizer was sent to a photodiode, which allowed both orthogonal polarization components to be detected. To test the half-wave operation of the PC, the output each PD viewed on directly on an oscilloscope. This allows for the voltage and timing of the HV pulses sent to the PC to be set, as the pulses should be completely flipped between the PDs with no signal on both PDs at any time. This scheme was also used for calibration once the entire instrument was built, specifically for the alignment of the PC to be checked and for the confirmation of factory benchmarks such as the contrast ratio, to be elaborated upon in Chapter 4.

## Lock-In Detection

One of the main reasons for modulating the polarization with a PC in this system was that it can retard the pulse polarization components at a fast user-defined repetition rate. This allows for the incoming optical pulses at 1 kHz to be modulated between linear polarization states or CP helicities on a pulse-to-pulse basis (500 Hz). This differs from other experiments and polarization resolved instruments which use a static polarization which is modified between experiments or processed to extract parameters like the CD [15]. By modulating the polarization at a fixed frequency, this allows for the use of frequency-resolved, or lock-in, detection methods. The lock-in amplifier (LIA) is a well-known device as it is commonly used to increase sensitivity in the detection setups of many pump-probe style experiments (including THz spectrometers) by extracting small signals present on top of large backgrounds. For this instrument we use the SRS 830 LIA, the internal processing of which is explained below, as it is the combination of PC and LIA operation that gives this instrument its high sensitivities.

The signal processing that occurs within the LIA can be simply explained in two steps: first the input signal is multiplied by a sinusoidal reference generated internally by the LIA (Eq. 2.17), then an extremely sharp low-pass filter is applied to the result (Eq. 2.18). The point of this method is to isolate the component of the total input signal (which consists of real signal and random noise) at a particular frequency. The multiplication creates sum- and difference-frequencies for all frequency components of the input signal:

$$\begin{aligned} V_{Mult} &= V_{sig}V_{ref}\sin(\omega_{sig}t+\theta_{sig})\sin(\omega_{ref}t+\theta_{ref}) \\ &= 1/2\ V_{sig}V_{ref}\cos([\omega_{sig}-\omega_{ref}]t+\theta_{sig}-\theta_{ref}) \\ &\quad - 1/2\ V_{sig}V_{ref}\cos([\omega_{sig}+\omega_{ref}]t+\theta_{sig}+\theta_{ref}) \end{aligned} \tag{2.17}$$

where $V_{sig}$ and $V_{ref}$ are the voltages, $\omega_{sig}$ and $\omega_{ref}$ are the frequencies, and $\theta_{sig}$ and $\theta_{ref}$ are the phases of the signal and reference waves, respectively. This multiplication is done in the time domain, so all the frequencies present in the input signal will produce sum and difference terms with the reference. The resulting sum and difference frequencies are then sent through an extremely narrow bandwidth low-pass filter, which removes all of the AC

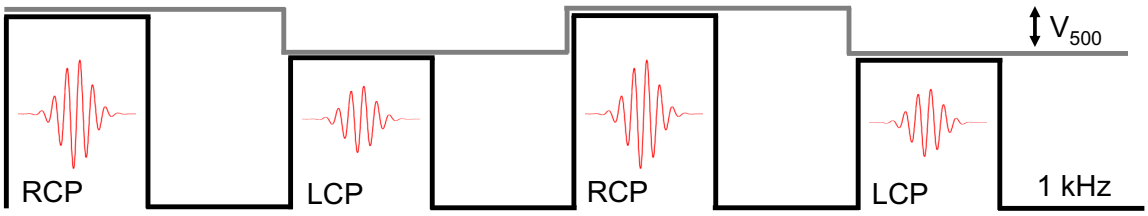


Figure 2.5: Pulse diagram showing the voltage extracted via lock-in detection in a circular dichroism experiment ($V_{500}$). Here the LCP component is more strongly absorbed by the sample, leading to less transmitted intensity and signal from the PD. By locking in to the modulation frequency, the LIA is able to directly extract the component at 500 Hz (gray line) with high sensitivity. This signal is directly the difference in transmission between RCP and LCP pulses, or the circular dichroism.

components of the multiplied signal. The only component of the input signal that will pass through this filter is the one at exactly the reference frequency, producing a a DC difference component:

$$V_{LIA} = 1/2\ V_{sig} V_{ref} \cos(\theta_{sig} - \theta_{ref}) \tag{2.18}$$

This output is linearly proportional to the amplitude of the input component oscillating at the reference frequency, while rejecting all other components of the signal and noise at all other frequencies. This frequency-resolved method allows for very precise measurements to be made even when the signal of interest (the one at the reference frequency) is 1000's of times smaller than other unwanted signals [42], as long as synchronization between that signal and the lock-in reference is maintained.

In principle, the LIA output is also dependent on the relative phase between the reference oscillation and the input frequencies, requiring the phase to be set such that the signal of interest is fully resolved. This can be overcome by utilizing a dual-phase LIA like the SRS 830. These devices have a second reference oscillator synced to the same frequency as the first, but with a 90° phase shift. This allows for both the in-phase and out-of-phase components of the signal at the reference frequency to be resolved at all times, and the two can be combined as $R = (X^2 + Y^2)^{1/2}$ to read off the total signal amplitude, regardless of phase, if desired.

This high sensitivity to signals at specific frequencies is why the fast modulation of the

PC is so important, by syncing the LIA to the modulation frequency of the PM line, the resulting DC voltage is a direct measure of the difference between the two polarization states measured by either a standalone or balanced detector setup. A simplified visual representation of this extraction in a CD experiment is shown in Fig. 2.5. This allows for a relative measurement to be taken just like the readout of the THz pulse field in time-domain spectroscopy and pump-induced change measured by the pump modulation LIA in time-resolved THz spectroscopy (see Sec. 3.1). In those cases the frequency component which is locked in to is imparted on the the beam (usually the THz) by an mechanical chopper, creating full on-off modulation that is resolved by the LIA. For the PM line, by modulating the polarization at the highest rate available ($f_{mod}$ = 500 Hz), we reject as much 1/f noise as possible while still gaining the benefits from lock-in detection, limited by the 1 kHz repetition rate of the amplified pulse train.

# Chapter 3

# Methodology

With the capabilities and physics of interest described above, the design and construction of this instrument will now be explained. First, the wide array of experiments now possible, some of which are detailed in Fig. 3.1, will be listed to show the full scope of this new tool. This is followed by a detailed breakdown of the design and construction of each beamline which makes these experiments accessible.

## 3.1 Acquisition Modalities

By bringing together THz spectroscopy and polarization-resolved detection, this instrument has inherited the ability to perform a multitude of different measurements. As such, a main feature of this setup is the flexibility in how each of these components are applied and combined. To show this, enumerated below are brief descriptions of the most interesting and potentially fruitful modalities and how they can elucidate the physics of 2D systems.

### Time-Domain Spectroscopy

The basis of THz spectroscopy measurements is the ability to probe a sample with a THz pulse and then glean full complex response functions (dielectric function, conductivity, etc.) from changes in the transmitted or reflected radiation compared to a reference. The simplest application of this technique is called THz Time-Domain Spectroscopy (TDS) [43].

Most simply, the source laser output is split into two beams, one strong and one weak: the strong beam is used to generate a THz pulse through one of a variety of methods (see Sec. 2.2.), and the other weak beam is sent to a delay stage to act as the sampling pulse. Once the THz pulse is generated it is focused onto the material to be measured using parabolic mirrors to avoid chromatic or spherical aberrations. Since the bandwidth in the pulse is

generally between 0.3-3 THz for OR generation in ZnTe, which corresponds to 100-1000 μm, the minimum spot size set by the Abbe diffraction limit will be approx. 0.2 $mm^2$, although the lowest frequency components may be limited to up to 2 $mm^2$ [7]. This focus is where the sample is placed, and after passing through the sample the beam is recollimated and focused into the detection apparatus. Here the optical gate pulse is used to sample the electric field of the transmitted beam. Since the duration of the optical probe pulse is much shorter than the THz transient, it can accurately resolve the evolution of the THz pulse electric field in time [43]. A delay stage is used to change the time between the THz and gate pulse on the fs scale so that the entire THz pulse can be sampled and changes in absorption or retardation induced by the addition of the sample can be accurately measured. Mechanical chopping is used on the THz beam in conjunction with lock-in amplification to measure the small THz-induced change (see Sec. 2.2) in the presence of larger noise, which could come from sources such as air currents, stray amplified pulse reflections, or laser power fluctuations.

To gain useful information from THz-TDS measurements, a number of trials must be done as the features of interest in the THz pulse are necessarily relative. Measurements are made with and without the sample of interest present so that a reference spectrum is available [7]. That reference spectrum could be taken through free space or through the substrate which the sample is attached to, depending on if the sample is freestanding or mounted. This allows for changes in the pulse only due to effects within the sample to be resolved, formalized in Eqs. 3.1 through 3.3. Analysis is done in the frequency domain by Fourier transforming the measured and reference pulses.

$$\frac{\tilde{E}_{sam}(\omega)}{\tilde{E}_{ref}(\omega)} = T(\omega)e^{i\phi(\omega)} = \tilde{t_1}\tilde{t_2}e^{\alpha d/2}e^{i(n-1)\omega d/c} \tag{3.1}$$

Here $\tilde{t_1}, \tilde{t_2}$ are the complex Fresnel transmission coefficients at the front and back sample interfaces, $d$ is the sample thickness, and $\omega$ is the THz frequency. The amplitudes and phases of each frequency component in the two spectra are in this way compared to extract information about the material's index of refraction $n$ and absorption coefficient $\alpha$ (in the

limit of low absorption coefficient):

$$n(\omega) = 1 + \frac{\phi(\omega)c}{\omega d} \tag{3.2}$$

$$\alpha(\omega) = -\frac{2}{d}\ln\left(\frac{(n+1)^2}{4n}T(\omega)\right) \tag{3.3}$$

These parameters can then be related to others such as the optical conductivity or dielectric function. Since this measurement directly records the THz field ($E$) and not its intensity ($E^2$), the amplitudes and phases of each frequency component are directly measured and thus both the real and imaginary parts of optical response functions can be reconstructed without having to use advanced analysis techniques such as Kramier-Kronig analysis [8].

## Time-Resolved Terahertz Spectroscopy

To observe out of equilibrium dynamics, a more advanced technique called Time-Resolved THz Spectroscopy (TRTS) [9] can be used.

TRTS shares many traits with THz-TDS, except for the addition of a third beam that acts as a pump pulse and another delay stage that permits delaying both THz generation and sampling beams with respect to the optical excitation. This allows for the parameters extracted from THz-TDS to be monitored as a function of time after an impulsive excitation. Another difference between the two experimental setups is the addition of a second mechanical chopper, this time in the excitation beam line. This chopper is set to half the frequency of the THz chopper, and allows for pump-on and pump-off measurements to be done in succession, recording both the pump-induced change and a reference measurement concurrently [44]. This minimizes possible artifacts in the measurement from laser power drift or timing instabilities that could influence the material response or the THz pulse itself, important for long scans.

To push systems out of equilibrium, a comparably high photon energy optical pump pulse is applied to excite carriers into higher-energy states, then the low energy THz pulse will be absorbed, reflected, or retarded if the carriers are mobile or have interactions in its bandwidth. A similar comparison as THz-TDS is recorded, but now considering the difference

between pumped and unpumped sample responses available as a function of the time after excitation $t_p$, with resolution determined by the time step set by the pump delay stage. For thin films or samples for which the optical pump is absorbed in a layer smaller than the THz wavelength ($d \ll \lambda_{THz} \approx 300\,\mu m$), the dynamic optical response can be extracted via Eq. 3.4 [7].

$$\frac{\tilde{E}_{pump}(\omega, t_p)}{\tilde{E}_{ref}(\omega)} = \frac{n+1}{n+1+Z_0\tilde{\sigma}(\omega, t_p)d} \tag{3.4}$$

Here $n$ is the substrate THz refractive index and $Z_0$ is the impedance of free space. This complex optical conductivity $\tilde{\sigma}(\omega, t_{pump})$ can be used to calculate parameters such as carrier concentrations $N$, scattering rates $\tau$, or effective masses $m^*$ via the conceptually simple but reliable Drude model [2, 7], shown in Eq. 3.5.

$$\tilde{\sigma}(\omega, t_p) = \frac{N(t_p)e^2\tau(t_p)}{m^*(t_p)} \frac{1}{1 - i\omega\tau(t_p)} \tag{3.5}$$

Looking at the change in THz pulse features between pump-on and pump-off cycles will provide not only the values enumerated above, but also how they change in time on the fs scale, giving a complete picture of the excited state dynamics of the system. This acquisition scheme leverages the high time resolution and consistent pulse train produced by modelocked laser systems to increase sensitivity and reduce measurement times in a scheme already uniquely able to measure ultrafast low-frequency dynamics [9].

## Circular Pump - THz Probe

The method most similar to THz spectroscopy, particularly TRTS, involves using the modulated beamline as a circularly polarized pump and measuring the dynamics of an induced change with a delayed THz pulse. The symmetry-breaking and transition selectivity imparted by the pump polarization allows the THz pulse, which has shown itself to be well suited for various dynamic carrier processes [11, 12], to probe the energy landscape with additional specificity. In materials with inequivalent valley selection rules, this scheme could be used to evaluate any differences between scattering times for carries in different valleys, shown in the left panel of Fig. 3.1. This could be performed without modulation if a singular transition is of interest, or the difference between valley physics could be monitored by the

THz transmission $\tilde{T}(\omega, t_p)$ after pulse-to-pulse pump polarization modulation is applied. The resulting signal is shown in Eq. 3.6.

$$\frac{\Delta\tilde{T}(\omega, t_p)}{\tilde{T}_0(\omega, t_p)} = \frac{\tilde{T}(\omega, t_p)^{\sigma+} - \tilde{T}(\omega, t_p)^{\sigma-}}{\tilde{T}(\omega, t_p)^{\sigma+} + \tilde{T}(\omega, t_p)^{\sigma-}} \tag{3.6}$$

Here $\sigma+$ is used to denote RCP pulses and $\sigma-$ is used to denote LCP pulses. In either mode of acquisition, lock-in detection helps improve sensitivity in measuring potentially small effects (see Sec. 2.4). Additionally, any gap opening effects induced by the breaking of time reversal symmetry can be monitored by the THz. If the gap is small enough to be in the THz range, direct transitions could be used as a way of measuring the size and dynamics of the gap. If the gap is large and free carriers are excited by the optical pulse, their dynamics as they relax around the new gap, whether they be relaxation or scattering, can also be probed by the THz pulse. The frequency resolution provided by THz spectroscopy can help identify the interactions between these carriers and other resonances in the system, providing more information into spin- and valley-dependent carrier dynamics.

## THz Pump - CD Probe

Reversing the roles of the pump and probe beams, the strong electric and magnetic fields of the THz pulse can be used to perturb and modify carrier distributions as well as other subsystems, depending on the resonance frequencies in the system and the strength of the field. The use of the THz field to induce spin splitting [45], which is then probed by circularly polarized light, is shown in the middle panel of Fig. 3.1. These fields can also impart non-negligable momentum and drive carriers to different points in the BZ [46], allowing selection rules in different parts of the energy-momentum landscape become accessible. As the parameters of the allowed transitions can change across momentum space, the measured transmission of circularly-polarized probe pulses $T^{\sigma+,-}$ can monitor if particular selective transitions have been enabled or quenched by this additional excitation, with a signal calculated as Eq. 3.7, similar to Eq. 3.6.

$$\frac{\Delta T(t_p)}{T(t_p)} = \frac{T(t_p)^{\sigma+} - T(t_p)^{\sigma-}}{T(t_p)^{\sigma+} + T(t_p)^{\sigma-}} \tag{3.7}$$

The band renormalization effect in graphene presented in Sec. 2.3 also apply here, especially

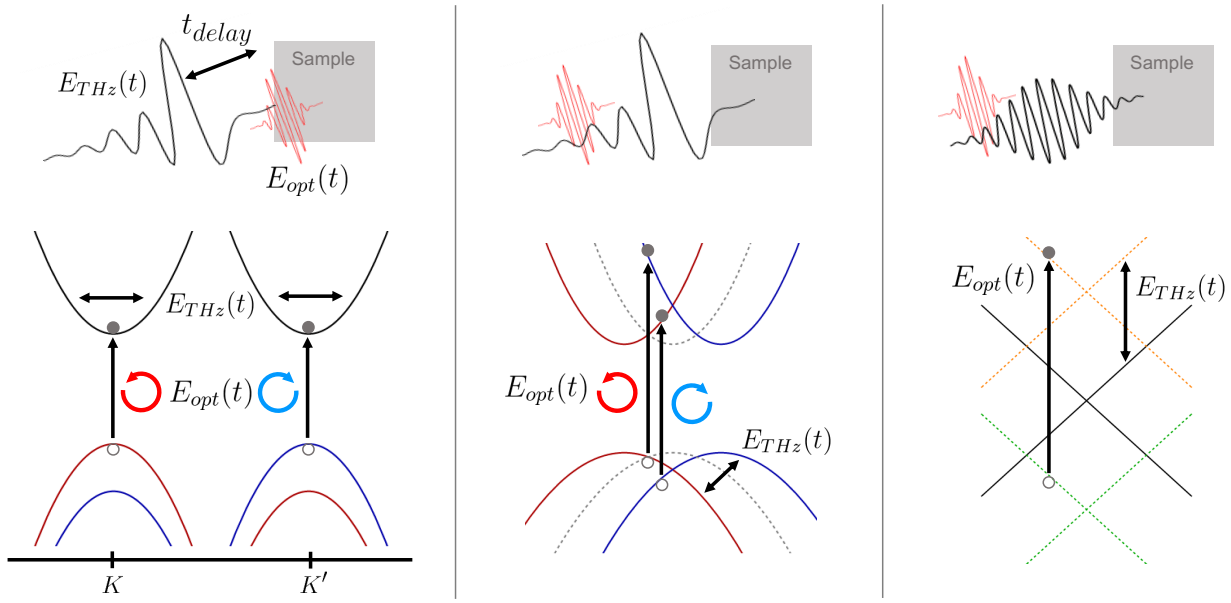


Figure 3.1: Band diagrams showing various possible experiment modalities: Valley-selective carrier mobility and scattering (left), THz-induced spin-dependent transition dynamics (middle), and periodically-driven Floquet engineering (right). Red and blue electron bands denote spin up and down states, respectively, and light helicities are marked by circular arrows. These examples, along with the other capabilities listed in this section, show the flexibility and wide range of interesting physics able to be induced and probed on ultrafast timescales.

in systems with nondegenerate spin bands. Additionally, materials whose band-edge physics is dominated by excitons on other quasiparticle interactions can be strongly perturbed by the strong THz fields, opening up another avenue for optical control and the measurement of carrier properties out of equilibrium and the relaxation therein. This is another way to open up THz to a range of spin- and valley-tronic applications.

### THz Pump - Polarimetry Probe

Similarly perturbing with THz, monitoring the induced ellipticity or rotation of a linear optical probe can reveal transient anisotropies in a material under influence of a strong electric field. This is the same style of measurement used to detect THz pulses in nonlinear crystals due to the electro-optic effect (see Sec. 2.2), but is sensitive to both the linear and quadratic field dependences (Pockels and Kerr effects), and can be detected in the same way with a balanced detection scheme (Eq. 3.8). This is of interest as some ordered materials

may react differently depending on which axis the excitation field is aligned to, and this can be probed by monitoring the degree of ellipticity induced in the probe beam [22].

$$\Delta\Phi(t) = \Delta n(t)\frac{\omega L}{c} = \frac{I_V(t) - I_H(t)}{I_V(t) + I_H(t)} \tag{3.8}$$

Here $\Delta n = n_e - n_o$ is the induced birefringence and $I_{H,V}$ represent the measured balanced photodiode signals after the modification of the probe beam via QWP and polarizing beamsplitter. By rotating the orientation of the THz excitation, sample, or probe polarization, these effects can be mapped out and the material's induced anisotropy can be recorded. Additionally, if the magnetic field component of the THz pulse is strong enough to sufficiently affect carriers or modify an applied static magnetic field, FR of the optical pulse could be recorded [47] by removing the QWP and measuring the orthogonal linear polarization components directly. The calculation of the rotation angle is given in Eq. 3.9 below, when discussing THz FR, but can also be calculated using Malus's Law, shown in greater detail in Sec. 4.3. This allows for the polarization resolved beamline to resolve a full suite of polarization effects with THz pumping: linear dichroism (diattenuation), linear birefringence (Kerr/Pockels effects), circular dichroism, and circular birefringence (Faraday effect).

### THz Faraday Rotation Spectroscopy

Similar to the resolution of optical rotation in the optical Faraday effect studies mentioned above, the polarization of THz radiation can also be resolved. By introducing a wire-grid THz polarizer after the sample, both linear components $(v, h)$ of the THz electric field can be recorded independently. The polarization angle can then be computed as Eq. 3.9. This can be performed both in a static THz-TDS style measurement or as a time-resolved probe monitoring rotation dynamics after various forms of pump excitation.

$$\theta \approx \frac{v/h}{v + h} = \frac{E_v(\omega, t_p)/E_h(\omega, t_p)}{E_v(\omega, t_p) + E_h(\omega, t_p} \tag{3.9}$$

This has already been shown without pump excitation in graphene, and quantized values of rotation have been observed in systems with [48] and without [49] irradiation by circularly polarized light, so there may be interesting quantum Hall experiment possibilities combining

the THz polarization resolution with circular pumping or vice versa. Like the anisotropy measurements, though, the physical adjustments required to resolve the different polarization components means that these measurements require more time then some of the others which can be fully automated.

## Circular Pump - Circular Probe

It can be beneficial to also perform degenerate experiments in the optical range to see the effects of phase space filling or absorption quenching, normally measured via photoluminescence [17]. By removing the THz generation optics, a strong optical pump can be applied to the material while still retaining the polarization sensitivity of the modulated beamline. This new strong pump can be modified in polarization and frequency through the addition of appropriate wave plates or filters. This allows for the selective pumping of carriers as in the Circular-Pump THz-Probe case, but with a degenerate probe sensitive the absorption difference between valleys. This can monitor inter-valley scattering and the volatility of valley populations [15], of great interest to those wanting to use valley populations for information storage. The recovered signal would be the same as for THz pumping, given by Eq. 3.7. This transformation of the THz line into another optical pump can be further applied to all the other modalities of the modulated line, further increasing the measurement possibilities with this instrument.

Also, circular polarization and its benefits are not only achievable in the optical regime. Through specialized wave plates THz pulses can also be circularly polarized, although this is difficult to achieve for broadband pulses. This ability, even for narrowband THz, opens up a new range for the symmetry-breaking effects to be applied such that any spin-dependent selections rules at low energies can be probed, with or without an additional pump excitation. With narrowband THz the time resolution is greatly degraded, but this may serve as a testbed for other more specialized instruments investigating the effects of circularly polarized THz on 2D material systems.

## Periodic Pump - Ultrafast Probe

In addition to all the dynamics able to be measured with the capabilities of circularly po-

larized light, the application of time-periodic electric fields opens up another dimension of transitions to be explored by creating copies of energy bands in energy-space [40]. These Floquet bands, described in Sec. 2.3, only exist while the periodic field is applied [19]. This makes them well suited for time-resolved measurements where the probe can be swept through the entire perturbation process, mapping out the evolution of the new band structure by monitoring transitions between band copies or the dynamincs of carriers excited within. An example of this experiment is shown in the right panel of Fig. 3.1. The bandwidth of the THz pulses can be narrowed to create more periodic strong driving fields, enabled by special THz bandpass filters. This type of excitation can also be combined with circular polarization, either on the periodic pump itself or on the probe, to induce gaps at the multitude of new band crossings within the dressed band structure [19]. The dependence of the Floquet states on the excitation frequency, intensity, and polarization [27] make this a powerfully tunable parameter that has yet to be explored fully in many interesting systems.

### Low-Temperature

The time resolved effects of band renormalization or splitting may occur on the meV scale, either due to the low energy of THz photons or the intrinsic interaction energy scales of the studied material, and as such keeping the thermal energy of the carriers low will allow for these small effects to be more reliably measured ($k_bT$ at room temperature $\approx$ 25 meV $\approx$ 6 THz). When this is required, this instrument is designed to accept a cold-finger cryostat outfitted with diamond windows, allowing for transmission studies at liquid nitrogen or helium temperatures without additional dispersion or absorption in both the THz and optical frequency range. This capability will also be useful in the study of valley lifetimes from selective polarized excitation, as control over the effective phonon population in the material may allow for additional understanding of the main relaxation pathways. This creates another new parameter that can be adjusted, and all of the effects presented previously could then be measured as a function of temperature, where phase changes, carrier localization, and other interesting effects can be measured and reliably controlled.

### Ultra-Clean Sample Surfaces

As this system's main purpose is to investigate the properties of material surfaces and topological states, the environment around the material surface must be considered as it may have dramatic effects on the physics present in these systems [10]. These modifications have the possibility to directly change how the material interacts with the electromagnetic probes used in this instrument, and as such should be accounted for. To accomplish this, the Grütter Surface Science Lab, also at McGill, has constructed a portable ultra-high vacuum (UHV) "suitcase". This suitcase can be attached to their larger UHV sample preparation chamber, allowing for the transfer of evacuated, annealed, or otherwise processed samples into its holding cell. Once the pristine samples are inside, the suitcase can be detached from the chamber and easily transported elsewhere, maintaining UHV conditions ($< 10^{-9}$ mbar). The suitcase has been outfitted with diamond windows so that its enclosure has no affect on the THz or optical pulses to be used to excite and measure the sample, and the OAPMs around the sample position in this instrument have been chosen to accommodate the insertion of this suitcase. As the samples in the chamber are free from contaminants and environmental adsorbants, this collaboration represents an opportunity for one of the first ultrafast optical studies of pristine material surfaces, since many laser-based spectroscopy tools operate in ambient or otherwise non-UHV conditions. Many materials have surface physics that may be affected by contaminants such as layers of water or other atmospheric molecules that are unavoidably present on samples measured in these conditions. This combination of tools therefore represents the first steps towards ultrafast measurements of surface physics in materials completely decoupled from their environment.

## 3.2 Beamline Design

As this thesis focuses on the creation of a new physical instrument, it is worthwhile to look in-depth at the design and construction process. While many of the design choices for this instrument are common in THz spectroscopy setups and will only be introduced in brief for completeness, several decisions were made considering the specific modalities of this instrument or limitations present in this lab and as such are worth discussing further. These include

the delay stage routing, multi-beam detection arrangement, and configurable beamlines. A schematic of the completed instrument is shown in Fig. 3.2, with the various beam paths represented by different colors. Following the main amplifier beam as it is split and tailored in different ways, the purpose, parameters, and features of interest for each beam will be enumerated below.

The amplifier beam, shown in red, is sent to the optical table which supports both this instrument and the previously-constructed ultra-broadband (UBB) THz setup. This beam is created by sending the modelocked output of a Coherent Mantis laser oscillator into a Coherent Legend Elite dual pulse duration, chirped pulse regenerative amplifier. The 300 mW oscillator output beam is chirped, selectively amplified, and recompressed, creating an amplified pulse train with a pulse energy of approx. 4.8 mJ centered at 800 nm (35 fs pulses at 1 kHz). This output is sent into a beamsplitter to split off 70% of this power to the UBB lines, then into a half-wave plate (HWP) and polarizing beamsplitter plate for power control. The reflected vertical polarization component is similarly sent to the UBB pump line, and the transmitted portion of the beam is now used to feed this instrument. This allows both instruments to operate at the same time, with the limitation that the UBB pump line and this instrument have a set amount of power that must be shared between them.

After the main line, shown in dark red, is established, it is sent back toward the amplifier for the division of the various beamlines required for this instrument. Along this long straight is where two alignment irises (not shown) are placed for the most sensitive adjustment of this instrument's alignment relative to the amplifier output. The optics in the diagram that do not interact with the marked beams were already present on the table for routing various beams to the UBB setup, and are shown as they presented restrictions to the beamline design explained below.

## Polarization Modulation Collinear Line

The first beam to be separated from the main line is the collinear PM beamline, which is split off by a 85% transmission, 15% reflection beamsplitter (85/15 BS). Taking the place of a the main pump line, this beam must be delayed with respect to the other lines to perform time resolved scans or other pump-probe measurements where the relative delay between the THz

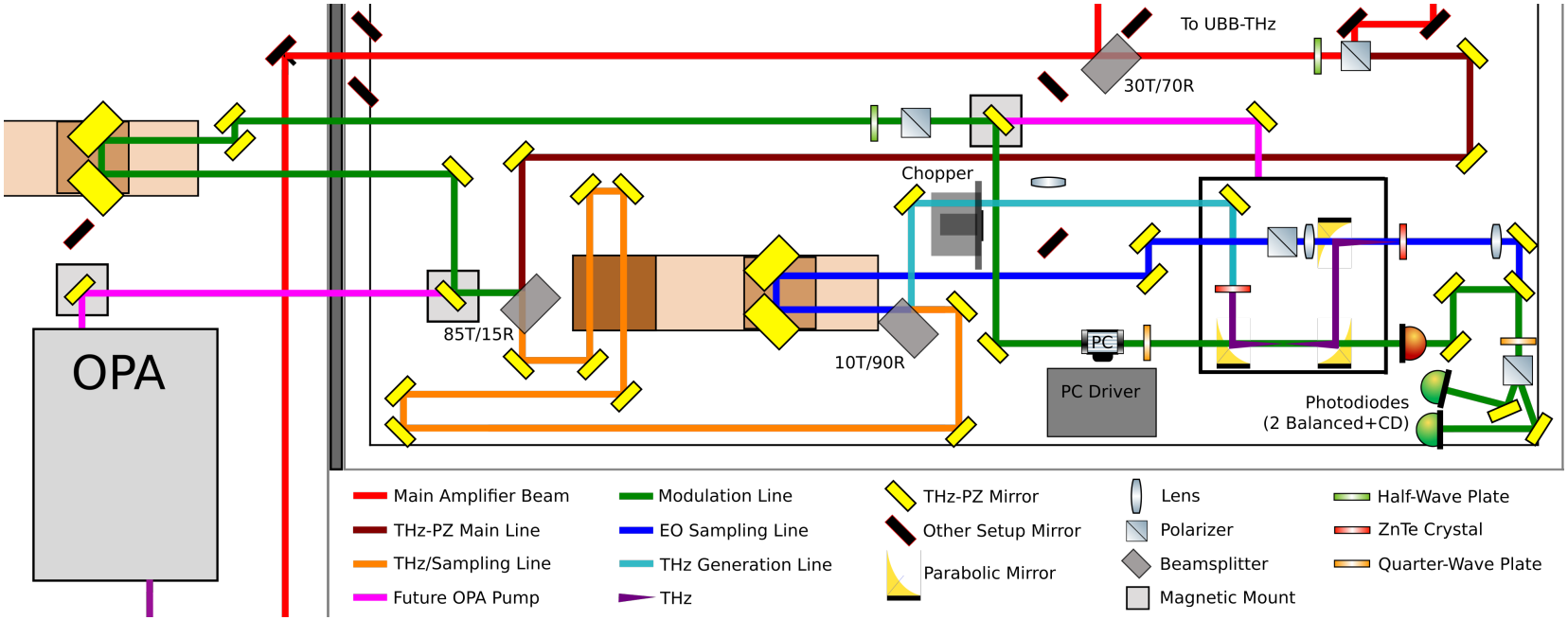


Figure 3.2: Detailed breakdown of beam routing from the regenerative amplifier. The output of a polarizing BS (top right) is used as the parent beam. The 85/15 BS separates the PM line and sends it to the pump-probe delay stage (left). The transmitted beam is further split by the 10/90 BS into the EO sampling and THz lines respectively. The EO sampling beam is then delayed by the sampling stage, allowing for the full THz waveform to be recorded. The PM line passes through holes in the OAPMs as a collinear pump or probe after being modulated by the PC, and can either be detected immediately after for CD measurements (orange PD) or can be sent to the balanced detection setup for polarization rotation recording (green PDs). Optics without beam paths are lines for other setups and restricted the possible designs of this instrument.

and PM lines must be adjusted. To accommodate other possible systems with resonances at frequencies away from the near-IR bandwidth of the amplifier pulses, this line can also be coupled to the output of an optical parametric amplifier (OPA). The OPA can convert the amplifier pulses to a wide range of output wavelengths (approx. 250 - 22,000 nm), and is coupled into the pump beamline by a removable mirror mount, shown in Fig. 3.2 as the intersection of the green and magenta beams. This was mainly incorporated for other experiments to be performed in this setup, but could also be used with the polarization modulation optics if material transitions at other wavelengths are identified.

The PM line is then directed into a delay stage and sent back to the far end of the table toward the THz generation and detection optics. This expanded geometry was necessary given that the delay stage used in this line is already in use for another THz setup. With one free delay stage to be used for the THz/sampling delay, this was the most easily accessible delay stage already present, and had to be accommodated. Before making its way into the PC arrangement, this beam passes through a HWP and linear polarizer, creating an effective power control for this line independent of the THz and sampling lines. This is critical as the power must be adjusted for the purpose of PM line: use as an optical pump requires higher powers to excite significant carrier populations, and lower power must be used if the beam is to be detected by the PDs to ensure they are within their linear output range. After power adjustment another removable mirror directs the beam to the PC; if removed the beam can be used to pump other experimental arrangements.

The PM beam is then directed through an aperture to reduce the beam size to 2 mm so it does not clip the entrance or exit ports of the PC. After passing through an optional QWP (depending on if linear or circular polarization states are desired), the beam passes through holes in the off-axis parabolic mirrors (OAPMs) used to direct the THz radiation. Between these mirrors, at the THz focus, is where the PM beam interacts with the sample. Matched focusing and collimating lenses can be inserted around the OAPMs to focus the PM line, guaranteeing a uniform interaction with the THz beam. After exiting the second OAPM, there are two possible detection arrangements. The first involves the whole beam impinging directly on a PD, shown by the Red PD in Fig. 3.2. This is useful for beam diagnotics as well as CD studies where absolute pulse intensities are detected to resolve differences in

absorption. For the resolution of LB or FR, mirrors couple the PM beam into the balanced detection arrangement after the ZnTe detection crystal used with the EOS line to measure the THz. A variable neutral density (ND) filter wheel (not shown) is placed along this routing to control the power into the photodiodes, allowing for strong interaction at the sample without saturating the detection systems, if required. LB can be resolved in the same way EOS is performed in THz detection, with the QWP and polarizer creating a balanced differential signal, or the QWP can be removed to resolve linear polarization rotation like that seen in KR and FR by detecting the orthogonal components directly. In principle, these additional optics may affect the absolute polarization state of the probe beam, but since lock-in detection allows for relative differences between pumped and equilibrium conditions or between polarization states to be isolated, this does not the diminish quality of the measured signal.

### THz Generation Line

After the PM pump line is split off by the 85/15 BS, the transmitted beam is statically delayed to make up for the long path lengths travelled by the PM line. This is necessary for the short pulses to arrive at the sample position at the same time, and for the delay stages to be able to sweep across this overlap point. This comes at the cost of multiple mirrors given the small available space, increasing the absolute number of optics required and the amount of instability therein. This beam is then split by a 90/10 BS into the THz and sampling lines, respectively. The reflected THz line is directed towards the top of the THz chamber, shown as the black enclosure in Fig. 3.2. An optical chopper can be inserted for modulated detection of the THz pulse, used for THz pump characterization or THz spectroscopy measurements. This location for the chopper is advantageous as it can be easily rotated from the THz line (light blue) into the PM line (green) if pump-on, pump-off studies with this beam are to be performed. The THz generation beam is then directed into the THz purge chamber, a $37 \times 28 \times 25$ cm box constructed from plexiglass which allows the entire THz path to be filled with dry air, removing the absorption and free induction decay normally affecting the THz pulses due to atmospheric water vapor [25]. All beams entering the purge box do so through appropriately-sized holes to not add additional delay or dispersion; the holes were found to be small enough as to not affect the purge quality (compare Fig. 5.1 to

Fig. 2.1).

The THz generation beam, once inside the purge box, impinges directly (unfocused) onto a 0.5 mm ⟨110⟩ ZnTe crystal, which generates THz radiation through optical rectification as described in Sec. 2.2. Directly after the ZnTe crystal, a Si wafer larger than the incident beam diameter is placed at an angle to reflect away any parts of the optical beam that were transmitted through the generation crystal. This Si wafer also reflects 30% of the THz pulse, but does not add any dispersion [8, 50]. The transmitted THz is focused at the sample position by the first OAPM, where it can interact or induce effects measured by the coincident PM line. If the THz is to be detected for spectroscopy or THz polarization rotation measurements, the second and third OAPMs recollimate and refocus the THz, respectively. The collimated portion is where a wire-grid polarizer can be inserted if particular polarization components of the THz are to be measured. The THz is then cofocused with the EOS line into another ZnTe crystal identical to the generation crystal for detection. The THz field is written onto the polarization state of the EOS pulse, and is measured with the balanced detection scheme that follows, described further in Sec. 2.2.

### Electro-Optic Sampling (EOS) Line

After being separated from the THz generation line, the EOS beam (dark blue) is sent directly into a second delay stage which allows the sampling beam to be delayed relative to the THz and pump lines. This allows for sampling pulse to be swept across the entire THz transient so that the full pulse electric field evolution can be recorded with fs time resolution. Both delay stages used in this instrument are Newport 150ILS-CC 150 mm linear delay stages with a minimum step size of 1 µm. This corresponds to a Nyquist sampling frequency of 71 THz, easily allowing for all THz components of the emitted pulse to be resolved. After being delayed, the polarization of the EOS pulses are ensured by a polarizer, then the beam is focused through the hole in the final OAPM. This beam is cofocused with the THz pulse, and after the nonlinear interaction in the ZnTe detection crystal, the EOS line is recollimated by a matching lens. The beam, now with a slight ellipticity if there was THz field present due to the induced birefringence in the detection crystal, is sent to a QWP and polarizing beamsplitter (Wollaston prism). The orthogonal linear polarizations are separated and fo-

cused into individual detectors for balanced detection. How this system resolves the THz field is covered in Sec. 2.2.

# Chapter 4

# Calibration

To characterize the abilities of this new system after the construction process, multiple tests were performed to check the operation of the new optics used for polarization modulation as well as the sensitivity of the instrument as a whole in measuring CD, LB, and FR. The measurement uncertainty present in absence of an expected response (baseline sensitivity) is taken to be minimum detectable change for these parameters and is compared to common responses and sensitivities reported in published studies.

## 4.1 Pockels Cell Optimization and Alignment

More so than most transmissive optics, the alignment of the PC is crucial to its proper operation. As the HV bias is applied across the optical axis of the beta barium borate (BBO) crystals to induce the index change that allows it to act as a wave plate, the incoming radiation must be well aligned with this axis for the retardation to be applied properly. Additionally, the HV amplitude must be set for the incoming wavelength range so the birefringence constitutes a correct half-wave rotation of the polarization.

The physical alignment of the PC first requires the incoming beam to be windowed such that it does not clip the entrance and exit apertures of the PC housing. This amounts to reducing the beam diameter to approx. 2 mm, which is accomplished simply with an iris as power is not a limiting factor in the line. This is done to prevent contact with the interior faces of the crystal. Once the PC housing and mount is adjusted to accommodate this beam without clipping, the fine alignment procedure can begin. This is done by placing the PC between two polarizers. The location of the transmitted beam is recorded on a card securely mounted after the analyzer polarizer and then the polarizers are crossed. Finally, a diffusing plate is placed before the PC to generate a large array of incoming wave vectors from the

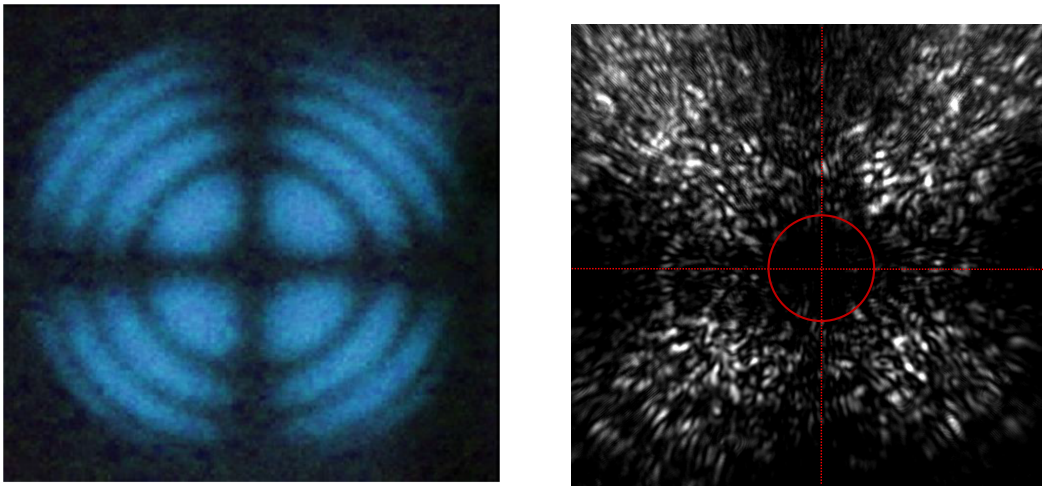

Figure 4.1: Examples of the dark cross and rings seen when aligning the PC and optical axes. The full pattern (left, reproduced from the manufacturer guide) is shown along with a close-up of the center cross (right) with the undispersed beam diameter and aligned position shown in red. The full pattern is visible in practice but an acceptable image could not be taken through the IR viewer, and the CCD sensor available is too small to capture the full pattern.

incoming beam; these non-axial wave vectors couple to the intrinsic axial birefringence of BBO and cause polarization modifications which are resolved by the polarizers [41]. This creates concentric dark circles in the resulting dispersed pattern described in Eq. 4.1.

$$k_x^2 + k_y^2 = \frac{\lambda}{L\ \Delta n}, \tag{4.1}$$

Here $\Delta n$ is the natural axial birefringence, $L$ is the length of the crystals, and $\lambda$ is the incident wavelength. This is superimposed onto a dark cross from the unaffected vectors that are blocked by the crossed polarizers. This pattern s resolvable by eye using a handheld IR radiation viewer, but a adequate photo could not be taken. The center cross region measured by a CCD camera is therefore presented with an example pattern taken from the PC manual in Fig. 4.1. Centering the pattern with the marked position of the undispersed beam ensures that the undispersed beam propagation is properly aligned to the crystal axes within the PC, as it sets the $k_{x,y} = 0$ point to be the beam transmission direction. The undispersed beam size and centering are shown via the red overlay in the right pane of Fig. 4.1, where the speckle pattern is enhanced over regular viewing on a less smooth, usually paper surface.

After the PC has been aligned to the beamline direction, the correct voltage from the HV driver must be set to ensure accurate polarization modulation. This is done in a similar arrangement to the physical alignment, but the resulting pulses are visualized on an oscilloscope after impinging on a PD. While the PC is on, proper operation causes the polarization to rotate 90°, which would cause maximum transmission through the crossed analyzer polarizer. This transmission is maximized by adjusting the HV output on the driver circuit. It was found for the provided driver that the HV plateaus around the half-wave voltage, making it difficult to determine if the PC is completely optimized. Additionally, the contrast ratio reported by the manufacturer (350:1) was not able to be completely reproduced (100:1) for the PC incorporated into the PM line. This will be addressed in the future and is elaborated in Ch. 6, but the quality of polarization modulation can still be tested with the LIA, the results of which are presented below.

## 4.2 Modulation Tests

To better confirm the quality of the polarization modulation, lock-in detection was used to measure the detection of signal in various modalities of operation. For these tests the 500 Hz (modulation) and 1 kHz (total signal) responses are both monitored; the unaffected input signal at 1 kHz is manually set to 10 mV and the LIA is measuring the full signal $R$ (see Sec. 2.4). The first test is an extension of the scheme used to initially align the PC, but includes cases where the PC on and rotating the polarization from horizontal (ensured by the input polarizer) to vertical every other pulse. This is to see if the full rotation of the pulse polarization from horizontal to vertical, as seen on the scope, is also resolved by the LIA. The results for a number of scenarios are shown in Fig. 4.2, where the standard deviation is computed from 100 individual measurements in each scenario.

Going from left to right, the blocked beam shows no appreciable signal at either frequency, as expected (this is true for all tests and will be assumed in the discussion of all following calibration tests). With the PC off there is maximum signal (10 mV) through the aligned (horizontal) polarizer and little signal through the crossed polarizer, limited by their extinction ratio and the presence of any scattered radiation making its way into the detector.

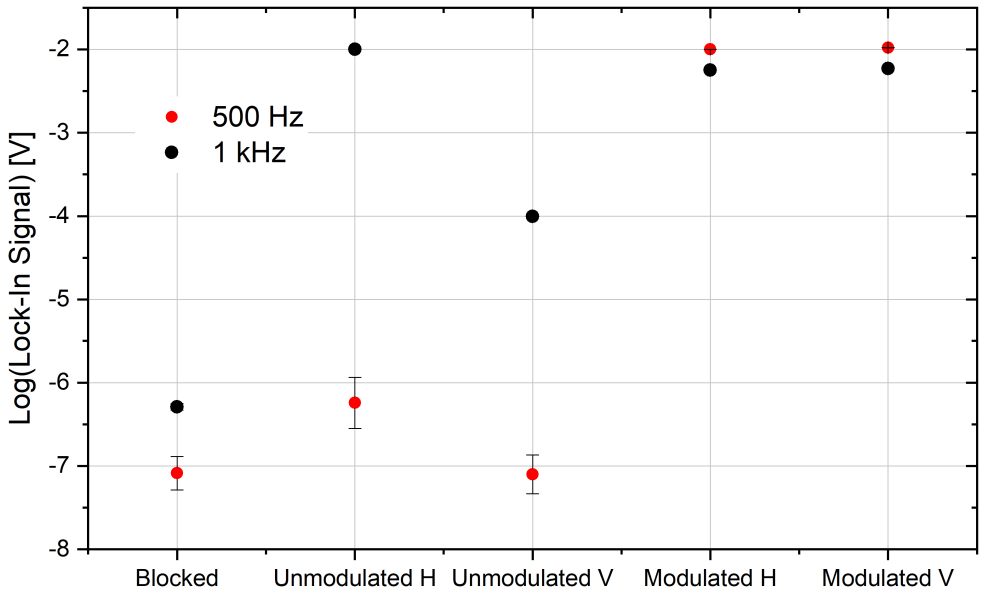


Figure 4.2: Results of the first test of the PC, linear polarization flipping without the addition of a QWP. Results are shown for no input beam, and for each analyzer polarizer orientation (horizontal or vertical) with the PC modulation both off and on. Measured signals for locking in to both 500 Hz and 1 kHz are shown.

This helps confirm the polarizer positions, and the lack of 500 Hz signal shows there are no other significant contributions at this frequency before the PC is turned on. With the PC modulating the polarization at 500 Hz the 1 kHz signal is consistently around half of the full scale signal, while the 500 Hz signal reaches approximately full scale (9.9 mV). This confirms that the pulses are being rotated from horizontal to vertical, as the polarizer blocks every other pulse making the full signal now only accessible when locked in to the modulation frequency. The pulse triggering the PC is the same one the LIA is referenced to, so when sensitive to the vertical pulse the signal is in phase with the lock-in reference, while when sensitive to the horizontal pulse the signal is 180° out of phase, matching expectations from the LIA signal processing description.

The second test also passed the resulting beam through an analyzer before measuring with the PD, but now a QWP is inserted after the PC to produce circularly polarized light. The QWP angle is set so that the power transmitted through a linear polarizer is the same for both orthogonal polarizer angles. This is also true of the 1 kHz lock-in signal, shown in the second and third columns of Fig. 4.3, and serves to confirm the acquisition scheme's accuracy

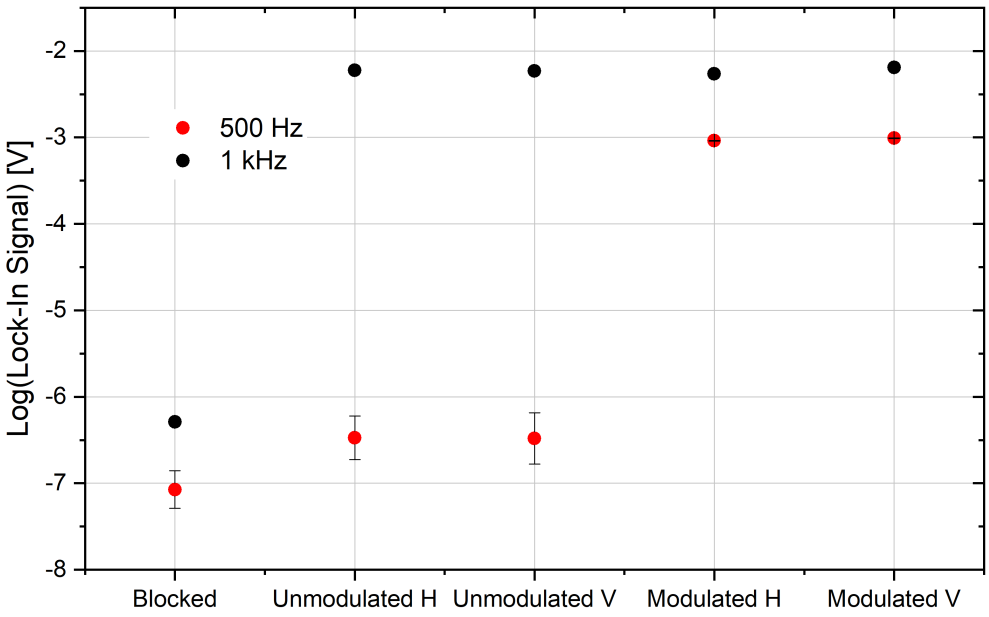


Figure 4.3: Testing the circular polarization quality by passing the helical pulses through a linear polarizer. Columns and datasets are the same as Fig. 4.2.

to equivalent measurements of transmitted power. When the PC is turned on, there is a small amount of 500 Hz signal (approx. 1 mV) for both analyzer positions that cannot be removed. There is also a noticeable difference in the 1 kHz signal between analyzer polarizer positions. These inconsistencies between RCP and LCP pulses are likely due to imperfect modulation caused by the large bandwidth of the PM line pulses, as the PC only can operate as a HWP for a single frequency, or in imperfect HV settings as explained above. The QWP is also optimized for a particular frequency, so some imperfect circular polarization and therefore modulated signal could arise from this as well, even with perfect alignment. This is likely the case as the insertion of a 3 nm bandpass filter improved these discrepancies, but cannot be used in real measurements since it severely limits the time resolution. While these signals affect the absolute measurement value, this offset is stable, and can thus be subtracted from time-resolved measurements as a static baseline. As shown in the next section, the sensitivity to time-resolved changes is still adequate given these offsets.

The final test is performed in the same arrangement that CD measurements will be taken: input polarizer, PC, QWP, and the detector with no analyzer polarizer. As such, this test only records the unmodulated and modulated responses at the two frequencies of

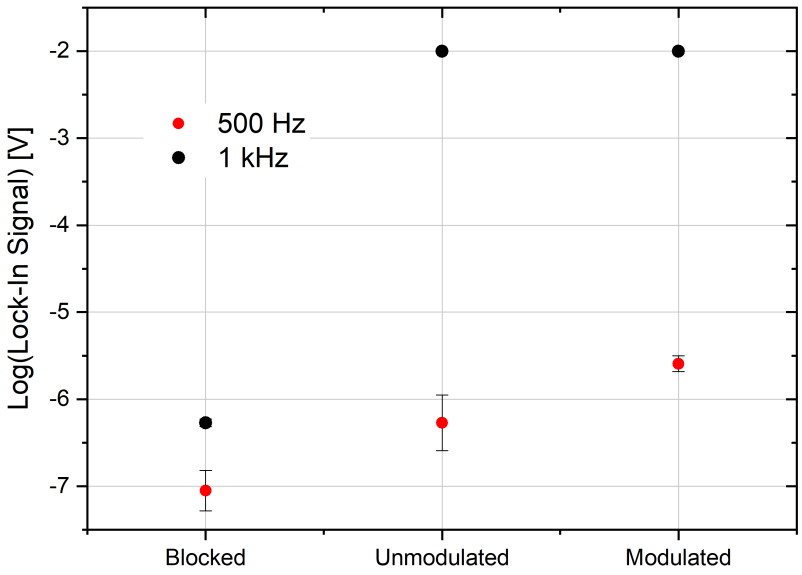


Figure 4.4: Circular polarization modulation in experimental conditions (no analyzer polarizer) with no beam, the unmodulated beam, and the modulated beam measured while locking in to 500 Hz and 1 kHz.

interest, shown in Fig. 4.4. For both scans the 1 kHz signal is the full signal, showing that no part of the beam is deviated when modulating with the PC. Additionally, the 500 Hz component has very little signal in general, showing only single μV's while the modulation is on. This could be due to slight differences in beam position due to the PC modulation, but is likely from electromagnetic interference picked up in the coaxial cables caused by the sharp edges of the HV pulses being applied. These do not affect other measurements significantly, but may have created this baseline which can also be easily subtracted in time resolved measurements.

These initial tests have shown that the initial alignment of the PC does carry over the LIA measurements, and allowed some inconsistencies to be identified that could not be otherwise. With these in mind, the next step to characterizing this instrument's performance is to measure the sensitivities of the multiple acquisition methods to see if they match other studies and reported responses.

## 4.3 Detection Sensitivity

Once the beamline timing and basic capabilities of the instrument were confirmed, the resolution of this instrument must be characterized for the various possible measurements that can be performed. These tests consist of configuring the instrument for the particular measurement (placing appropriate optics, routing to the correct detection setup), acquiring the data through the correct LIA arrangement, and processing the extracted signal into the quantity of interest. This will performed for CD (differential circular absorption), Kerr Effect (birefringence and ellipticity), and FR (linear polarization rotation and circular birefringence). All sensitivities are presented as a null measurement with any constant offset being subtracted off before plotting, as this makes the sensitivity easier to see and is a common procedure for time-resolved measurements.

### Circular Dichroism

As it is a measure of differential absorption, the calibration of CD is the simplest to perform, and thus will be used as the introduction to these calibration measurements. The main figure of merit is the sensitivity, represented by the standard error of the mean for measurements made in the absence of any effect. This baseline sensitivity will be compared to other studies on similar materials using similar experimental methods and analyses to confirm that this system has the resolution required to sense the effect in question. Often these effects are small changes superimposed on top of larger effects such as laser power fluctuations, steady-state absorption and reflection, and other confounding processes. This is why lock-in detection and modulated detection are used, to remove as much random noise and fluctuations from other sources as possible.

For CD measurements, the PM beam is sent directly into a single PD, and the polarization helicity is modulated between RCP and LCP. The difference in measured signal between these two states represents the CD present, and is intrinsically measured by a LIA referenced to the triggering frequency of the PC, as explained in Sec. 2.4. To compare to other relative measurements and correct for long scale power drifts (due to laser power fluctuations, thermal effects, etc.), this quantity is normalized by the total incident radiation. This leads the

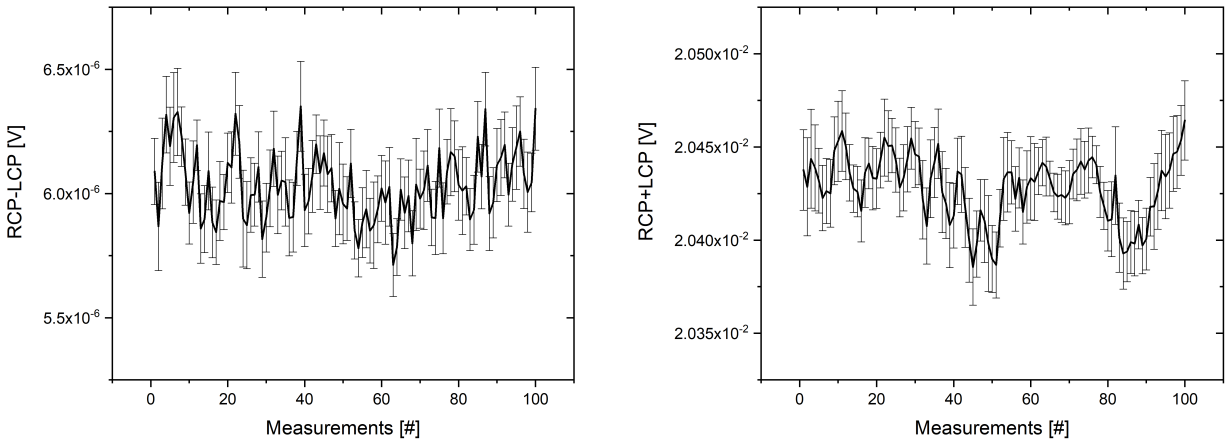


Figure 4.5: Means and standard errors for 100 point scans with no sample. Statistics are based on 20 individual scans. The 500 Hz differential signal (RCP-LCP) shown on the left is divided by twice the 1 kHz signal (RCP+LCP) shown on the right to get the true CD signal.

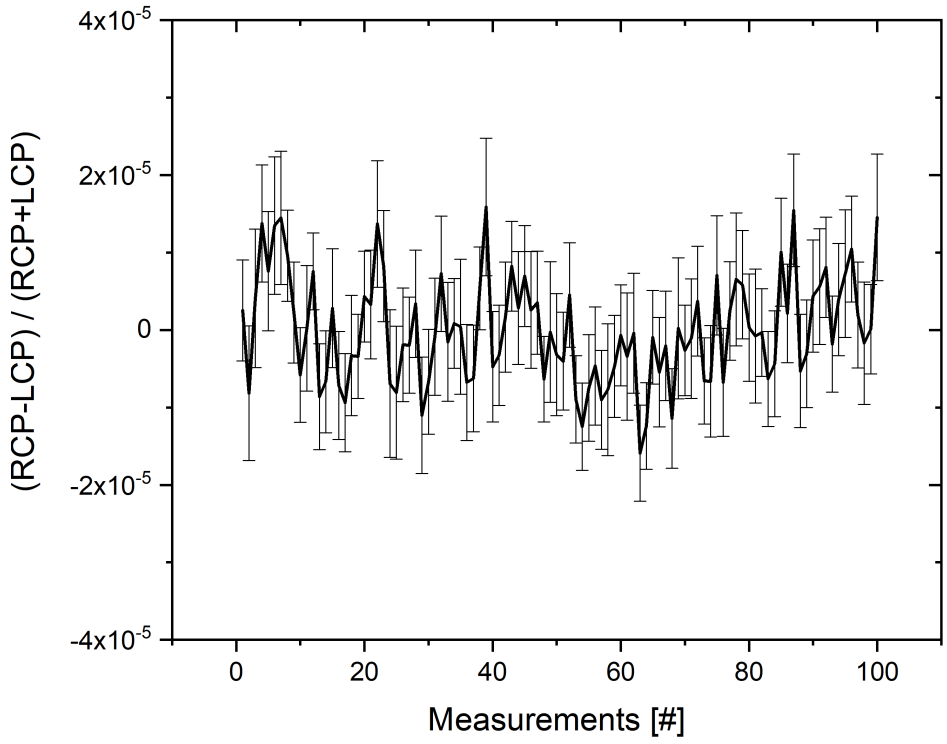


Figure 4.6: Computed mean and standard error for CD = (RCP-LCP)/(RCP+LCP). The calculated standard deviation of approx. $3 \times 10^{-5}$ sets an upper limit on the individual scan sensitivity, while the standard error of the mean of approx. $7 \times 10^{-6}$ shows the improved measurement sensitivity with averaging. This plot has had its baseline subtracted, as would be done to show true time-resolved changes in a sample measurement.

calculated value for CD shown in Eq. 4.2.

$$CD = \frac{RCP - LCP}{RCP + LCP} = \frac{LI_A(500\ Hz)}{2 \times LI_A(1\ kHz)} \tag{4.2}$$

Here $LI_{input}(frequency)$ is used to represent the signal extracted from lock-in detection for either A (single input) or A-B (differential) inputs. The normalized CD is computed by taking the differential signal and dividing by twice the 1 kHz signal. The factor of two is required as the 1 kHz signal represents the average signal of each pulse impinging on the PD, so representing the full value of $RCP+LCP$ requires twice this value. These two datasets could be acquired in multiple different ways: either by using one LIA whose reference frequency switches between 500 Hz and 1 kHz or by using two LIAs with one set to each frequency. The choice here is essentially equivalent, but there can be a preferred choice if other experiment parameters like pump excitation necessitate specific schemes due to the limited number of LIAs available and able to be accommodated in this setup.

To model the time-resolved nature of many measurements of interest with this system, the measurement noise was characterized by taking multiple 100 data point scans, which were then processed to find the variation over this range. This type of measurement could represent the time before excitation in a time-resolved study, and the variation of the null signal gives the absolute sensitivity of the acquisition method. The raw data collected in these scans while locking in to 500 Hz and 1 kHz are shown in Fig. 4.5. These are then processed into the final CD measurement shown in Fig. 4.6. For all calibration measurements the error bars represent the standard error (SE) calculated from 20 individual scans.

It is found that the absolute sensitivity of a single measurement, represented by the standard deviation (STD), is approx. $3 \times 10^{-5}$ for this acquisition mode. There are a large range for reported values of measured CD, with signatures from $10^{-2}$ [51] to $10^{-6}$ [52], and others at all orders of magnitude in between [53–55]. This range makes it difficult to determine a single value that constitutes adequate sensitivity, but the measured standard deviation places the sensitivity of this instrument's measurements at a place where most of these reported effects would be resolvable. Additionally the SE, representing the confidence in the computed mean value, is a factor of $\sqrt{N}$ smaller, decreasing with the number of measurements used in the

average. For this calibration $N = 20$ which leads to a SE of approx. $7 \times 10^{-6}$, a high degree of certainty for this type of measurement as shown by the cited sensitivity range. This test confirms that the sensitivity gained through modulated polarization and subsequent lock-in detection is high enough to measure CD in the types of materials to be studied with this instrument. Additionally, the automatic recording of data allows for many scans to be taken, improving the SE if the result is especially small.

## Kerr Effect and Ellipticity

The second mode of acquisition measures induced ellipticity. This style of measurement is natural given that the effect of THz radiation in OR detection is exactly this effect. In that case the THz field couples to the electro-optic properties of the detection crystal to produce a transient birefringence which is measured via balanced detection, and the same strategy will be used here. Any induced ellipticity in the PM beam is converted into an imbalance between the linear components of the probe after the QWP, and is detected similarly to CD with differential sensitivity. The left plot of Fig. 4.7 shows the scan sensitivity for the acquisition mode that is used for THz detection. These data are calculated identically to the CD value, but with the numerator resulting from a differential measurement which subtracts the responses from the balanced photodiodes before extracting the signal at the reference frequency.

$$\Delta\phi = \frac{H - V}{H + V} = \frac{LI_{A-B}(500\ Hz)}{2 \times LI_A(1\ kHz)} \tag{4.3}$$

This expression shown in Eq. 4.3 directly represents the phase retardation $\Delta\phi$ caused by the birefringence of the sample [22]. The sensitivity achieved is very similar to the CD tests with a STD of $3 \times 10^{-5}$ rad and SE of $7 \times 10^{-6}$ rad, showing the robustness of the lock-in detection for different methods of signal input. Measures of sensitivity in this modality have not received the same attention as CD or FR/KR studies and as such less examples of experimental resolution are available. But again a general range between $10^{-3}$ [56] and $10^{-6}$ [31] rad is presented, mainly from those also using this scheme for EOS. These figures show the instrument at present performs on par, also confirmed by its ability to resolve THz pulses with similar fidelity as the EOS line (see Fig. 2.1 or Ch. 5).

This mode of acquisition can also be used with polarization modulation. Instead of mea-

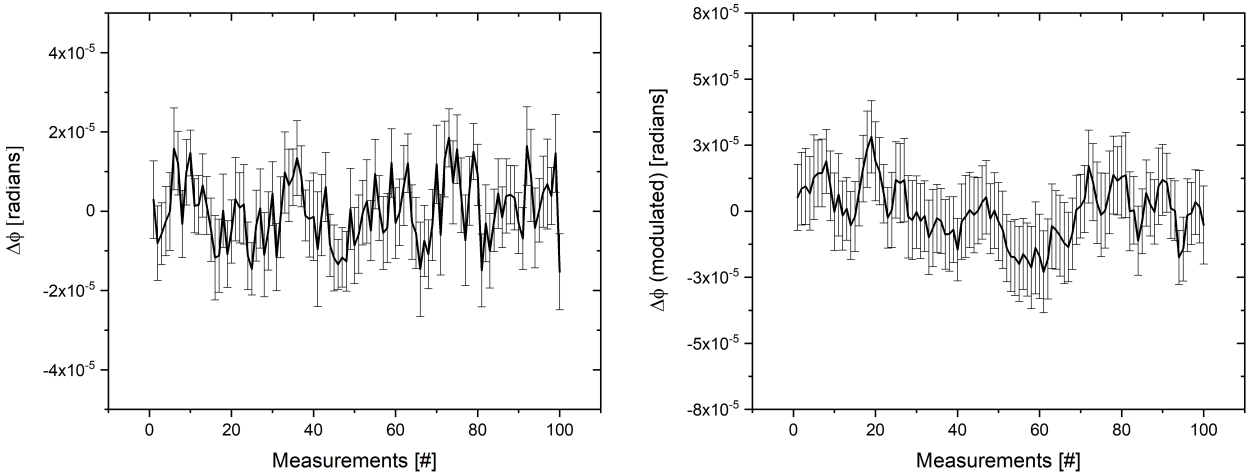


Figure 4.7: Means and standard errors for the ellipticity sensitivity measurements. Both locking into a chopped pump excitation (left) and polarization modulation (right) are tested, showing similar sensitivities. While the normal measurement probes the induced birefringence, the polarization modulated measurement probes the difference in birefringence seen between orthogonal linear polarization states.

suring the pump-induced change to the materials indices of refraction, now the instrument is sensitive to the difference in the birefringence measured between orthogonal polarizations. This type of measurement is not usually performed, but could have uses in rotational studies of anisotropic samples or other materials with unique electro-optic properties along each axis. There is more significant offset in this measurement than the non-modulated one since the signal is being modulated at the detection frequency, and is largely due to imperfect balancing or modulation due to the large bandwidths necessary for producing short pulses. This is again easily subtracted in real measurements, and it is found that this mode has similar sensitivity, with a STD of $6 \times 10^{-5}$ rad and a SE of $1.3 \times 10^{-5}$ rad. The slightly larger STD is likely due to the larger signal offset and may be able to be improved through achromatic optics or more dynamic range in the PC driver (see Ch. 6).

## Faraday Effect and other Polarization Rotation

The final type of polarization-based measurement this instrument has been designed to measure is polarization rotation. Instead of creating ellipticity in the polarization like linear birefringence, circular birefringence results in an in-plane rotation of incident linear polarization (or a rotation of the ellipse axis in the case of incident elliptical light). This is commonly

observed in magnetic materials or those under the influence of strong magnetic fields, and can be used to investigate a wide variety of effects related to the intersection between quantum hall effects and topological states [57,58] as well as the degree of electron spin orientation [59]. In the optical regime, this is measured using the balanced detection setup without the QWP, probing the incoming linear polarization state directly.

The rotation of the linear polarization state can be extracted by monitoring the angle of the polarization, which after passing through the beamsplitting polarizer in the detection setup is recovered as Eq. 4.4, based on Malus's Law for the intensity passed through a polarizer.

$$\Delta\theta = \frac{1}{2}\arccos\left(\frac{2LI_A(500\ Hz)}{LI_A(1\ kHz) + LI_B(1\ kHz)} - 1\right) \tag{4.4}$$

This measurement cannot benefit from the modulated polarization scheme as the circular birefringence affects both linear polarization states in the same way, and the other available methods are insensitive to small index differences between modulated CP helicities. Lock-in detection can still be used to extract the difference between pumped and unpumped cases by chopping the excitation or perturbation, though, improving sensitivity for the time-resolved studies of interest here. With this calculation, the STD of the measurement shown in Fig. 4.8 is approx. $3 \times 10^{-3}$ rad, giving this instrument mrad sensitivity in extracting the FR angle. The SE improves this sensitivity to the single-mrad level, which is on par with measurements taken in other FR studies [49, 56] showing effects in the $10^{-1}$ rad to $10^{-3}$ rad range. This sensitivity is lower than the previous modes of operation due to the additional processing required to extract a field polarization angle from an intensity measurement, but is still acceptable.

This same effect can also be resolved in the THz regime, in which case a wire-grid polarizer inserted after the sample position can be used to resolve the orthogonal polarization components $E_V$, $E_H$ of the transmitted THz radiation [49]. By adjusting the EOS polarization and detection crystal orientation to compensate, the ellipticity sensitivity presented in the previous section can be applied to the rotation of the THz polarization, albeit no longer achievable in a single measurement due to the physical optic adjustments required. The FR is directly extracted by measuring the amplitude of the two orthogonal components [58], a more simple measurement (Eq. 4.5) since when detecting THz through EOS the field

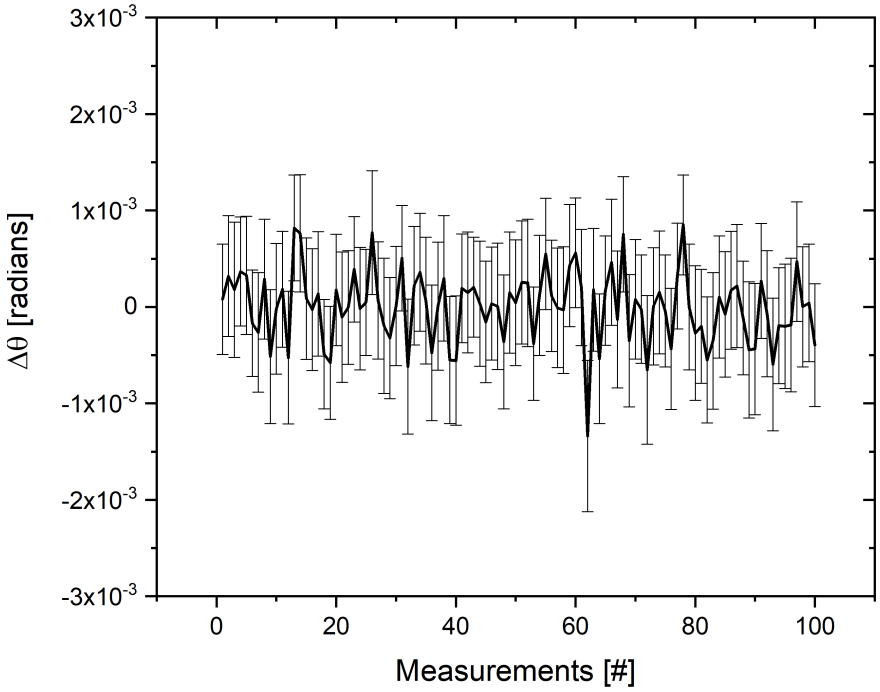


Figure 4.8: Means and standard errors for polarization rotation sensitivity measurements. This allows access to the circular birefringence properties many materials exhibit in the presence of magnetic fields, and could be resolved in time using the magnetic field component of the THz pulses generated in this instrument.

itself is directly measured. Utilizing the THz in these studies has the additional benefit of accessing frequency-resolved FR within the bandwidth of the pulse [60], and inherits the same sensitivity as the other LB measurements.

$$\theta(t) \approx \tan(\theta) = E_V(t)/E_H(t) \tag{4.5}$$

Overall, the sensitivities reported for the various acquisition modes align with those reported in literature and are thus able to measure effects such as CD, LB, and FR. The noise on these measurements could stem from two main sources: the LIA itself or the quality of the optics employed in the detection apparatus. At the lock-in sensitivities utilized for these signals (10's of mV to 1's of μV), neither the input noise nor the analog-to-digital conversion noise are appreciable [42]. The lower limit of approx. $10^{-5}$ on the sensitivity of the measurements is therefore likely due to the polarizers in use to characterize functionality and detect signals of interest. Both the linear polarizers used to ensure linear input polarization and

the Wollaston polarizer used to separate linear components in the balanced detection scheme have an extinction ratio of 1:100,000. This corresponds to an ability to distinguish polarization states with $10^{-5}$ sensitivity, and is likely the limiting factor for these measurements. While this is seen to be acceptable compared to other studies, this could be improved by the addition of further cleanup polarizers, and is an option that will be explored if experimental signatures are found to be too small for the instrument in its current iteration.

## 4.4 THz Pulse Detection and Time Resolution

While the measurement of polarization-resolved effects is a major capability of this system, the time resolution ultrafast pulses provide is another key aspect. To confirm this facet of the instrument, the first goal during construction was to simply generate and detect THz pulses, as this allowed for beamline alignment, timing, and detection to be checked at the same time. This was first done with the EOS beamline and allowed for the THz pulses produced in ZnTe as well as the balanced detection scheme to be optimized. With this confirmed, focus could be shifted to the properties of the PM line. The main concern was if the short pulses produced by the amplifier had been stretched in time, which could occur due to a number of thick and dispersive optical elements like the calcite polarizers and BBO crystals within the PC.

The first check was to monitor the THz pulse now through the PM line, using it in place of the EOS line used before. If the additional optics dispersed the optical pulse significantly, then the detection resolution would be degraded and the THz electric field measured would not match the one measured in the non-dispersed EOS line, in both time and frequency space. This was measured in the case study of the ZnTe detection crystal, with results in time and frequency space shown in Fig. 5.1. The time-domain THz waveform shows no smoothing over of fast features and the frequency resolution does not appear to be degraded between the two lines with the same scan parameters used, which indicates that the polarization optics in the PM have not significantly broadened the pulse in time.

As a second measure, additional dispersion was checked for via second harmonic generation in a nonlinear BBO crystal. As the nonlinear second harmonic generation scales with the

incident power, the amount of blue light generated acts as a measure of the peak power, directly related to the pulse duration. The pulse duration can be manually varied by adjusting the compressor grating angle just before the amplified pulses exit the amplifier, allowing for deviations from optimal compression to be noted, which would indicate significant dispersion introduced by the polarization optics. The baseline was set by optimizing the generated THz field. As the THz generation is also maximized for the shortest pulse duration, the compressor angle for peak THz emission is taken to be the maximally compressed case as there are fewer dispersive materials in the THz line. It was found that the compressor angle which optimized blue light generation was not significantly different than for the peak THz, within 1-2 steps of the stepper motor controlling the grating angle. As the peak THz generation did not vary within this small range, the compressor angle was set to maximize the second harmonic generation, ensuring the shortest possible pulse in the PM line. This test, combined with the equivalent THz detection, confirms that the PM line's time resolution has not been significantly reduced by the addition of the polarization optics, and will be quantified with future autocorrelation measurements (see Chapter 6).

# Chapter 5

# Case Study: Pockels Effect in ZnTe

With the individual capabilities of the instrument quantified, a preliminary study to characterize the performance in measuring polarization effects in a real material was performed. In this case, a material exhibiting time-resolved polarization effects is already present: the ⟨110⟩ ZnTe detection crystal. This crystal has been widely used for THz generation and detection via OR since the technique was applied to THz detection [31], and as such the interactions within are well-understood. This material will be used to confirm the operation of this instrument as a whole in both common and modified modalities.

## 5.1 Traditional THz Detection

The first test of the PM beamline via this material is to reproduce the THz detection done with the EOS beamline, similar to the time-resolution tests done before. In this case the PM beamline acts as the sampling pulse which records the instantaneous THz field. By scanning the PM line delay stage, the relatively short PM pulse can be swept across the stationary THz waveform. The THz electric field will be imprinted on the polarization ellipticity of the optical beam and is then measured as an intensity difference on the balanced photodiodes. An optical chopper inserted into the THz beamline allows for the polarization change induced uniquely by the THz pulse to be extracted via lock-in detection, referenced to the frequency of the chopper, in this case 500 Hz.

A trace of the measured THz waveform using the PM line is shown in the left panel of Fig. 5.1, superimposed upon the same THz pulse measured in the same detection crystal using the EOS beamline. These scans are normalized to show the differences between the two detection lines other than different absolute intensities of the detection pulses. Both traces were measured in ambient conditions without purging the THz chamber with dry air.

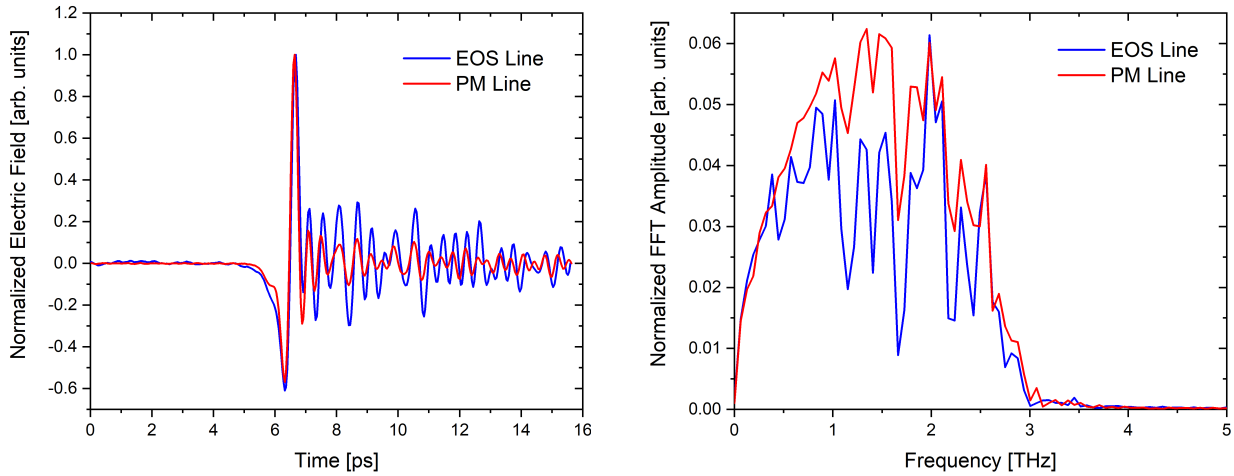


Figure 5.1: Comparison of normalized THz pulse waveforms (left) and spectra (right) measured in ambient conditions by the EOS as well as PM beamlines. Both lines capture all THz frequencies, but the EOS data have signatures of the greater THz path length.

This causes differences between the pulses: the oscillations seen after the main THz pulse are stronger in the EOS-detected pulse, most readily seen in the time-domain traces. This is due to the different length the THz pulse travels in air before being detected; when using the PM beamline the THz only travels to the sample position since this is the point of interaction between the THz line and the colinear PM line, whereas when using the EOS line the THz travels through the sample position to the detection crystal, over twice the distance. This path difference affects the THz waveform due to the presence of water vapor in the ambient environment. Water vapor has multiple absorption resonances in the 1-3 THz range, with the strongest at 1.69 and 1.71 THz [25], on top of being a polarizable polar molecule that exhibits free induction decay upon being oriented by the transient THz field.

The effect of water absorption is most readily seen in the frequency domain. By applying a Fourier transform to the time-domain pulses, the water absorption lines are clearly visible when compared to a THz pulse generated and detected in a dry-gas-purged environment (see Fig. 2.1). These absorption features are more pronounced in the EOS-detected pulse, as expected for a longer path length and thus longer exposure of the THz pulse to atmospheric water. Additionally, the frequency range resolved by the two different detection lines is the same, further proving the PM line's time resolution and interaction with the THz at the sample position are adequate.

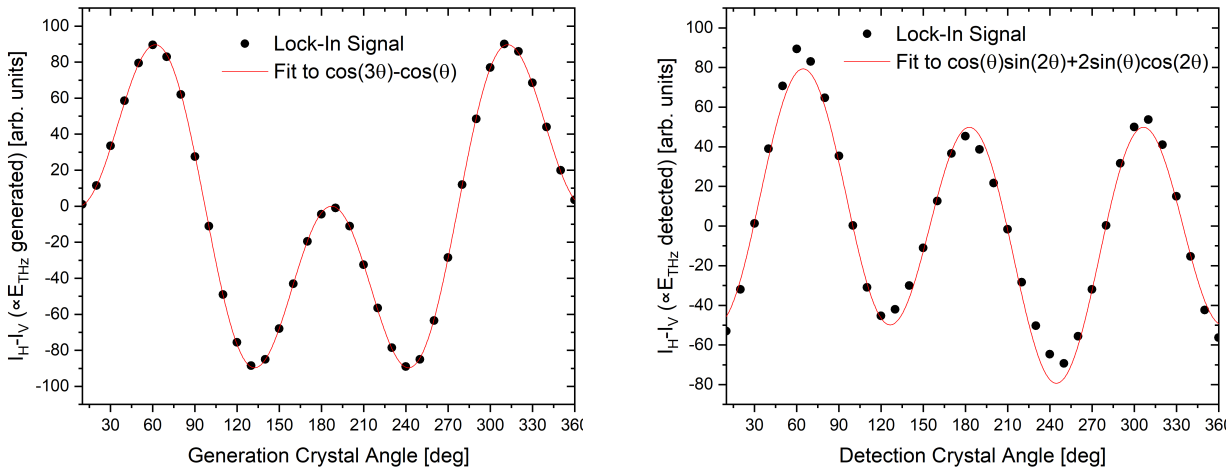


Figure 5.2: Measured peak THz field as a function of generation (left) and detection (right) crystal angle. Red lines are fits to the functional dependencies predicted from OR theory [20, 61].

To further characterize ZnTe with the PM beam, a rotational study was done on both the detection crystal and the generation crystal. The results are shown in Fig. 5.2. Both the generation and detection efficiency in ZnTe are highly dependent on the relative angle between the incident optical polarization, THz polarization in the case of the detection crystal, and the crystallographic axes of the ZnTe, as discussed in the prior section on optical rectification (Sec. 2.2). Each crystal is optimized for maximum detection efficiency before the rotation study and only one crystal is adjusted at any one time to decouple their rotational dependencies.

The data presented in Fig. 5.2 is taken with the PM beam sampling the peak THz field, and shows its variation with the corresponding crystal angle. The left plot shows almost perfect agreement to the theoretical prediction for the magnitude of the induced polarization as the azimuthal angle of the generation crystal is changed [61], which directly modulates the amplitude of the radiated THz field. A similar test is done for the detection crystal azimuthal angle, which fits reasonably well with the expected functional dependence presented in ref. [20]. This treatment is based on predicting the induced change of the index for various axes in the ZnTe crystal, and thus demonstrates the power of the balanced detection scheme, and by extension the modulated lock-in detection, in resolving changes in polarization. These are also the basis of performing LB and RF measurements, and as such act as initial demonstrations of this ability.

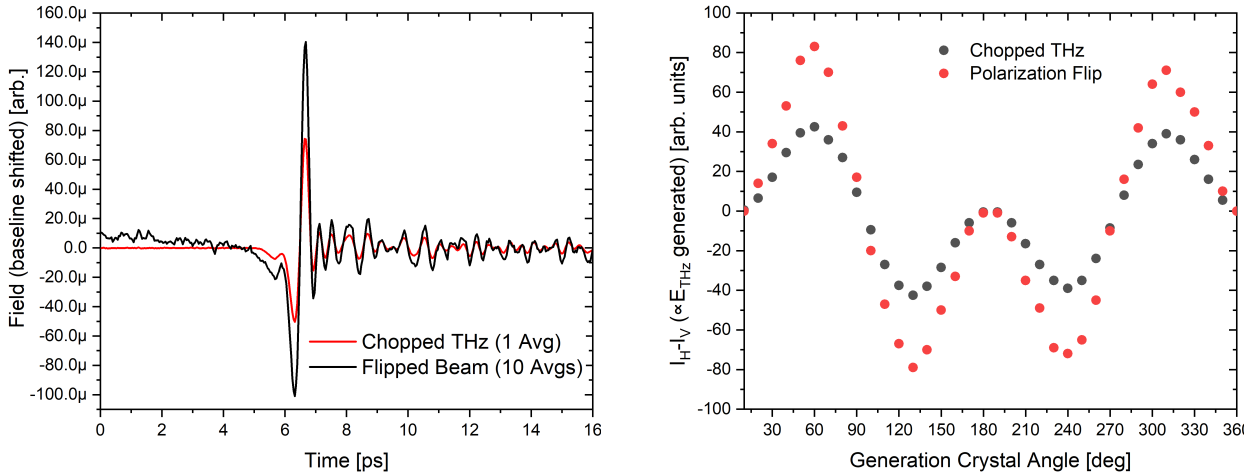


Figure 5.3: Comparison between unmodulated acquisition and measuring while locked in to the polarization modulation, both for entire THz waveforms (left) and peak field generation as a function of crystal rotation (right). Doubled signals are recorded for both tests, as expected for a differential linear polarization flip in ZnTe.

## 5.2 Modulated Detection

To incorporate and test the new polarization modulation capabilities of the PM line, the PC is introduced, allowing for half-wave retardation (horizontal-to-vertical or RCP-to-LCP) to be applied to pulses in the PM line with individual pulse selectivity as discussed in Sec. 2.4.

To demonstrate the tangible effect of this modulation in the spectrometer, ZnTe was again used as a well-known sample. In this case, the modification of the probe beam's linear polarization via the PC changes the interaction between the THz and optical fields in the ZnTe crystal. The rotated pulse resulting from the PC with HV applied selects a different component in the electro-optic tensor $r_{ij}$ to determine the interaction, and should show that change in the trace of the THz pulse seen as the delay stages are scanned. The theoretical treatment of the detection process presented in Planken et al. [20] shows that the symmetry of ZnTe dictates that the strength of the interaction (magnitude of the electro-optic tensor) is equal, but with a sign change in the value selected when the probe is perpendicular to the field. When combining this difference with the LIA detection scheme used with balanced detection, one expects to see twice the measured signal for the same THz pulse, as locking into the modulation frequency of the PC (500 Hz) allows for the extraction of the difference between signals measured with the PC on versus off. This is the effect seen when integrating

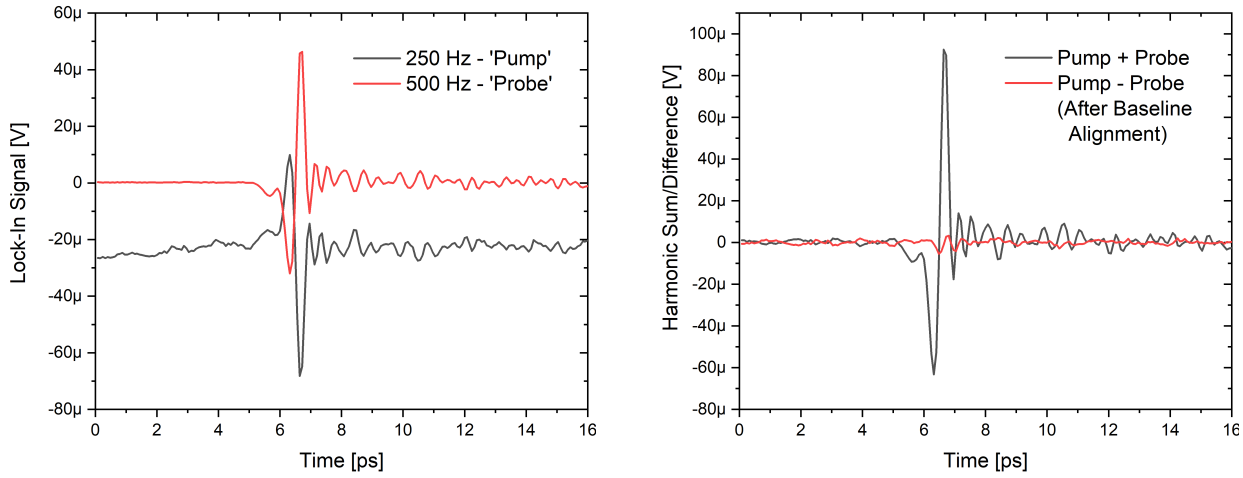


Figure 5.4: TRTS dual LIA acquisition showing the waveforms recorded at 250Hz/500Hz (left) and their sum and difference (right). Summing the signals gives the THz induced change in ZnTe birefringence, and subtracting gives a running baseline, all in a single scan.

the PC, shown in Fig. 5.3. Both the measured THz waveform (left) and peak THz measured as a function of generation crystal angle (right) show twice the signal as the same effects measured with unmodulated detection methods. The increase in noise seen in the modulated tests is due to the LIA now being sensitive to the 500 Hz flip only, not the changes brought upon uniquely by the THz excitation. This will be improved upon in the TRTS acquisition test explained below. In this scheme, overall factors of -1 (whether the PC on state results in positive or negative signal) can be accounted for by adjusting the lock-in phase or by monitoring $R = (X^2 + Y^2)^{1/2}$. This test helps confirm the PC's half-wave operation, as well as the use of polarization modulation in a TDS-style acquisition scheme, where steady-state reference measurements and PC diagnostics can be performed.

The next step is to demonstrate a TRTS-style double-modulation measurement where one would like to compare pumped and unpumped responses as a function of delay between excitation and probing beams. This is most easily achieved with two LIAs, one referenced to the 500 Hz modulation of the polarization line, and the other referenced to the induced change which is to be chopped at 250 Hz. In this ZnTe sample the excitation is the THz itself. The result of this acquisition is shown in Fig. 5.4.

It is clear that an equivalent double signal is recovered in this acquisition scheme as well after processing. This time the original signal is directly measured in the 250 Hz component,

and must be added together with the similar 500 Hz signal to get the true pump induced change (after removing the baseline and inverting to account for the difference in phase). This processing is common in double-modulated detection schemes, such as those used by the UBB THz spectrometer also situated in Cooke Lab. Additionally, the subtraction of the two signals gives the baseline or unpumped signal, another benefit of this acquisition scheme that allows for changes in the unpumped behavior to be tracked in addition to the pumped effects. The small oscillation present in the baseline signal of Fig. 5.4 demonstrates this, as it is a weak THz transient generated in the ZnTe detection crystal by the probe beam. Since it is not modulated at the pump frequency, it is not included in the pumped signal and can be monitored independently. The absolute value of the electric field is different between these tests and the TDS demonstration due to different incident powers in the probe beam and LIA sensitivities to compensate, likely caused by daily differences in the amplifier power output. This TRTS demonstration, with the previous results from the TDS measurements and rotational studies, shows that the polarization modulation induced by the PC acts as expected in a known material and thus can be applied in future THz pump-probe style experiments.

Overall, the measurement of the well-known ZnTe sample shows that that even with the slight inconsistencies found when optimizing the PC, the system performs as expected in both unmodulated and modulated modes of operation. This serves as a proof of the instruments capability, and as such it can now be used to start measuring other materials, particularly those showing interesting surface physics, with the wide variety of modalities available.

# Chapter 6

# Conclusions and Future Work

This thesis represents the conceptualization and building of a new type of THz instrument with specific focus on detecting polarization effects such as circular dichroism, induced ellipticity, and Faraday rotation with sub-picosecond resolution in both the THz and optical ranges. By combining polarization modulation through the use of a Pockels cell, lock-in signal acquisition, and flexible detection schemes, a variety of potential experiments become available with high sensitivity. The new polarization modulated beamline is able to detect THz pulses with the same quality as the electro-optic sampling line, and is sensitive enough to measure polarization signal reported in the literature ($10^{-5}$ for circular dichroism, $10^{-5}$ rad for linear birefringence, and $10^{-3}$ rad for Faraday rotation). Pulse-to-pulse polarization modulation by the Pockels cell is also confirmed with calibration tests and through study of an electro-optic material, ZnTe, which shows polarization-sensitive THz-induced birefringence. To use these capabilities, two-dimensional and topological materials show novel spin and valley physics that can be affected by these particular polarization states and high THz fields, making them prime candidates for study. Therefore, this instrument represents a new way of leveraging ultrafast THz pulses as both an excitation and probe in experiments to measure spin and orbital dynamics in materials. To further quantify and improve the performance of this instrument, some future checks and modifications are presented below, followed by a brief description of some initial experiments already slated to utilize the new functionalities of this tool.

## Future Augmentation and Characterization

In order to remove the dependence of this setup on the UBB pump and improve the beam quality overall, we plan to insert an additional beamsplitter into the main amplifier line before the UBB optics. This will also give more control over the length of the main line, allowing

for the additional delay mirrors in the THz/sampling source line to be reduced, decreasing the number of optics used and improving overall stability. Separating the beams at this point also allows for more power to be utilized in the THz generation, important for generating the highest possible fields to strongly perturb systems.

To achieve higher THz fields, required for perturbing many of the systems with large exciton binding energies or field strength-dependent splitting or gapping, other generation methods must be employed as the fields produced by ZnTe are not currently intense enough. As an example, the interaction energy of the approx. 1 kV/cm field with the excitons in an $MoSe_2$ monolayer amounts to a $< 0.1\%$ change compared to the binding energy, not enough to induce any appreciable changes. Also, higher fields create opportunities to create meV-scale gaps in Dirac materials, or widen and shrink band gaps by 100's of % (see Sec. 2.3), which could be dynamically measured. To increase the generated fields in this instrument, the ZnTe generation line will be modified to incorporate tilted pulse-front optical rectification in $LiNbO_3$ [62]. In this material the phase/group indices are too different to produce efficient THz when travelling collinearly, but can create a THz wake propagating away from the excitation pulse at an angle, similar to Cherenkov radiation. To account for these factors, optimal generation therefore calls for a tilted pulse front and special crystal cut angles so that the THz emitted from the optical pulse propagates constructively and exit the crystal properly. This tilt is most often achieved using a reflection grating, for which the reflected pulse is imaged onto the crystal to create a pulse whose tilt matches the wake angle of the generated THz. These additional optics will inhabit the same space now used to route the beam from the initial polarizing beamsplitter, which will be empty due to the earlier separation of the THz-PM beam from the UBB lines.

Regarding the PM line, while the time resolution was qualitatively confirmed to not be significantly impacted by the additional optics, it will be necessary to have a quantitative measure of the pulse duration to determine the absolute time resolution for time-resolved experiments. This has proved difficult considering the cramped nature of the optical table around the PM line and the fact that the beam power allowed through the PC is not enough to be measured in the single-shot autocorrelator present in the lab. As the main beamline is moved, a small autocorrelator will be built in the free space to measure the true duration of

the PM beam pulses. Additionally, the current HV output from the PC driver does match the full range specified by the manufacturer, and plateaus around the half-wave voltage point. This makes the optimization of the PC voltage difficult as the true best voltage for these pulses may be currently inaccessible. While the PC appears to be working well given the outcome of the calibration tests and ZnTe study, the cause of this inconsistency is currently being investigated with the help of the manufacturer to ensure optimum operation in the future. Finally, if spectrally-resolved optical absorption measurements are required in future tests, a small grating monochromator system could be built, allowing for wavelength selectivity to be incorporated into current measurements without loss of sensitivity.

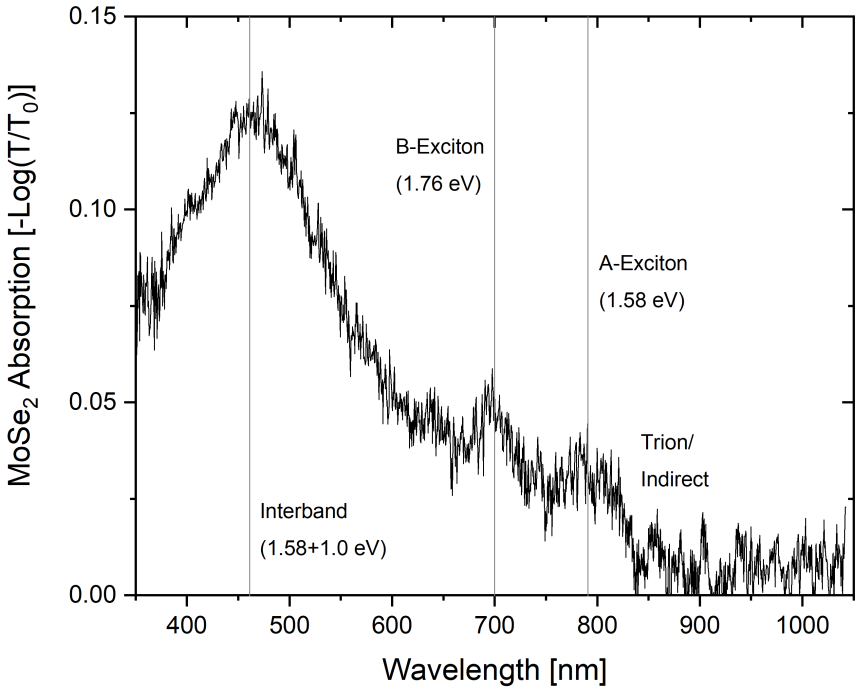


Figure 6.1: White light absorption spectrum of an $MoSe_2$ monolayer. The absorption peaks shown correspond to the A- and B-excitons formed when exciting from either of the spin-split bands, as well as the excitation of free carriers (exciton resonance energy plus binding energy). These absorption features are unique to monolayers [63].

## First Experiments

Now that this instrument has been built and characterized, it can begin to measure materials of interest. There are already a number of materials that are to be investigated with this system; the motivations behind these choices are explained in brief below.

One potential sample is graphene. Many different researchers and techniques are still

being applied to this material which exhibits a wide variety of interesting physics such as linear energy-momentum dispersion, large conductivities [64], Hall-like anomalous currents [48], and topologically protected edge currents [65]. The interactions between large THz fields and graphene's properties have been investigated [14,49], but few have utilized the time resolution of THz pulses to measure how these effects are modulated by polarized excitation or how they evolve over time. Additionally, access to pristine graphene surfaces through the vacuum suitcase (see Sec. 3.1) allows for prior studies on graphene to be confirmed, or to quantify the effect of environmental exposure if it is present. This has the potential to impact much of the current work on graphene, as how it reacts in various environments as well as the dynamics of carrier responses therein will be important for future applications in real-world electronics. We intend to first measure conventional quantities such as conductivity in the presence of different environments, then proceed to see if the application of different polarizations of light can affect the properties measured by THz, or if the THz can affect the band properties measured by the optical pulse, in these specific environments.

Another material well-suited for investigation is $MoSe_2$, a TMD whose monolayer direct band gap [63] is within our optical pulse bandwidth. This system's excitation physics is dominated by strong excitons, and has valley-dependent spin splitting allowing for transitions to be selectively excited [15]. With the circular polarization capabilities of this new system, the carrier dynamics of individual valley parameters such as conductivity and scattering rate can be measured with TRTS. A monolayer sample was already tested in this instrument as a preliminary investigation and trial of the system (monolayer nature confirmed by the absorption spectrum shown in Fig. 6.1), but the current THz fields are too weak to significantly modify the excitonic physics due to their high binding energies. The intense ($> 100$ kV/cm) THz pulses from the $LiNbO_3$ generation process will be able to drive these systems strongly, opening up possibilities for THz ultrafast control of intervalley transport and the surveying of different physics across the Brillouin zone [46]. These systems have also shown large nonlinear optical responses [51], which could be probed with the polarization modulation beam after intense THz pumping. Understanding these interactions via this new instrument may open doors for the large family of TMD monolayers as well as other topological materials, some of which may hold the keys to further advancement in material physics.

# Appendix A

# Acquisition Example

This section presents the details of acquiring data in an experimental setting, from the physical adjustments and checks needed to the software recording of measured signals, to give a better understanding on how repeatable time-resolved scans are achieved. As the data collection scheme is largely reliant on software written for other THz instruments by prior students in Cooke Lab, this is given as an appendix to not interrupt the explanation of the work done specific to the new polarization-resolved setup that is the focus of this thesis.

In order to make reliable measurements for a wide range of experiments, precisely controlling the two delay stages in tandem is crucial. For example, in a spin-polarized pump - THz probe experiment, long sweeps of the sampling pulse to measure the entire THz waveform are performed between small steps of the pump delay stage to map out the post-excitation response. This requires the absolute stage positions of the THz-sampling overlap on the sampling delay stage and pump-THz overlap on the pump stage to be known. Once the THz pulse is located in time/position in air during calibration, delay estimates based on the index of the sample are used to find it in the presence of a material. Next, to find pump-THz overlap, a sample which has a strong THz response to pumping (such as Si or GaAs) is measured, allowing the precise arrival time of the pump to be found by monitoring the change (if the pump arrives before) or lack thereof (if it arrives after) in the THz pulse. Once the pulses are aligned in both time and space, the experiment is planned as to what time resolution is required at different timescales after excitation and whether the entire THz pulse must be extracted or just a singular point. This is dictated by the expected timescale of relaxations after the pump excitation as well as if the material is dispersive to THz. Once decided, the acquisition software controls both the LIA settings required to resolve the signal of interest and the stage motion. As both the universal stage controller and the LIAs are capable of communicating via GPIB, a LabVIEW virtual instrument is used to control both

the stage motion and data capturing. This software has been built up to provide a number of important features for automating complex experiments, the most important of which are enumerated below.

The first notable benefit of the LabVIEW environment is the ability to control all lock-in settings through the software. This makes switching between different experiments or acquisition modes fast and simple, and effectively creates a flexible acquisition tool that can be modified to create dynamic experiment-recording schemes. For example, if an experiment requires both the 1 kHz and 500 Hz components of an input signal to be monitored, say for normalized CD measurements, the system can switch between the second harmonic of the 500 Hz reference signal and fundamental for each measurement point. Thus both responses can be recorded at the same time by the same piece of equipment. This modification can be applied in multiple ways to a variety of parameters to increase the possible measurements for a single LIA. This is important as there may be many frequency components to be monitored for a particular measurement (250 Hz pump, 500 Hz modulated probe, 1 kHz reference), which would typically require a large number of LIAs. The automation of acquisition parameters reduces the number of hardware devices required for measurement and prevents the input signal from being unnecessarily divided multiple times, which can complicate analysis when the individual LIA signals are recombined and processed.

For time-resolved measurement, correct pulse overlap/delays and subsequent data recording is crucial, and thus makes up the other facet of this software environment. Precise steps of each stage can be controlled so that a map of the response, THz or otherwise, can be recorded and repeated with fs resolution. Multiple scan ranges and resolutions can be programmed in arbitrary orders for resolving fast and slow components of effects without oversampling leading to long measurement times. For example, it is possible to automatically record 10 scans of a THz waveform every 20 fs after pump excitation for 200 fs, then every 50 fs for the next 800 fs, then every 200 fs for the following 4 ps. Additionally, the software automatically plots the recent scans for easy identification of signals while setting up experiments, and on-screen markers read out positions in time and delay stage distance for easy marking of points of interest. Finally, all of the measurements are automatically recorded as individual data files as well as an average file, so that both quick diagnostic viewing and full analysis are

able to be performed directly from the data files written. The files contain all of the relevant experiment parameters (stage positions and relative delays, LIA settings, time and date) so that even if scan logs are lost or incorrect the measured data can be analyzed and interpreted accurately. These files are standardized such that reliable and repeatable analysis scripts can be used for extraction of relevant material parameters and measured effects.

# Bibliography


[1] Felix Bloch. Über die quantenmechanik der elektronen in kristallgittern. *Zeitschrift für physik*, 52(7-8):555–600, 1929. 1

[2] Paul Drude. Zur elektronentheorie der metalle. *Annalen der physik*, 306(3):566–613, 1900. 1, 26

[3] Edwin H Hall. Sommerfeld's electron-theory of metals. *Proceedings of the National Academy of Sciences of the United States of America*, 14(5):370, 1928. 1

[4] K V Klitzing, Gerhard Dorda, and Michael Pepper. New method for high-accuracy determination of the fine-structure constant based on quantized hall resistance. *Physical Review Letters*, 45(6):494, 1980. 1

[5] Kostya S Novoselov, Andre K Geim, Sergei V Morozov, D Jiang, Y Zhang, Sergey V Dubonos, Irina V Grigorieva, and Alexandr A Firsov. Electric field effect in atomically thin carbon films. *Science*, 306(5696):666–669, 2004. 1

[6] Ankur Gupta, Tamilselvan Sakthivel, and Sudipta Seal. Recent development in 2d materials beyond graphene. *Progress in Materials Science*, 73:44–126, 2015. 1, 14

[7] P Uhd Jepsen, David G Cooke, and Martin Koch. Terahertz spectroscopy and imaging–modern techniques and applications. *Laser & Photonics Reviews*, 5(1):124–166, 2011. 1, 4, 6, 8, 10, 24, 26

[8] David G Cooke. *Time-resolved terahertz spectroscopy of bulk and nanoscale semiconductors*. Ph.d, 2007. 1, 4, 8, 25, 37

[9] Matthew C. Beard, Gordon M. Turner, and Charles A. Schmuttenmaer. Terahertz spectroscopy. *The Journal of Physical Chemistry B*, 106(29):7146–7159, 2002. 1, 6, 25, 26

[10] Hassan A Hafez, X Chai, Y Sekine, M Takamura, K Oguri, I Al-Naib, MM Dignam, H Hibino, and T Ozaki. Effects of environmental conditions on the ultrafast carrier dynamics in graphene revealed by terahertz spectroscopy. *Physical Review B*, 95(16):165428, 2017. 1, 32

[11] David A Valverde-Chávez, Carlito S Ponseca, Constantinos C Stoumpos, Arkady Yartsev, Mercouri G Kanatzidis, Villy Sundström, and David G Cooke. Intrinsic femtosecond charge generation dynamics in single crystal ch3nh3pbi3. *Energy & Environmental Science*, 8(12):3700–3707, 2015. 1, 4, 26

[12] Yang Lan, Benjamin J Dringoli, David A Valverde-Chávez, Carlito S Ponseca, Mark Sutton, Yihui He, Mercouri G Kanatzidis, and David G Cooke. Ultrafast correlated charge and lattice motion in a hybrid metal halide perovskite. *Science advances*, 5(5):eaaw5558, 2019. 1, 4, 26

[13] H Hirori, A Doi, F Blanchard, and K Tanaka. Single-cycle terahertz pulses with amplitudes exceeding 1 mv/cm generated by optical rectification in linbo3. *Applied Physics Letters*, 98(9):091106, 2011. 1, 2, 5, 9

[14] Hadi Razavipour, Wayne Yang, Abdeladim Guermoune, Michael Hilke, David G Cooke, Ibraheem Al-Naib, Marc M Dignam, François Blanchard, Hassan A Hafez, and Xin Chai. High-field response of gated graphene at terahertz frequencies. *Physical Review B*, 92(24):245421, 2015. 1, 5, 63

[15] Nardeep Kumar, Jiaqi He, Dawei He, Yongsheng Wang, and Hui Zhao. Valley and spin dynamics in mose2 two-dimensional crystals. *Nanoscale*, 6(21):12690–12695, 2014. 2, 14, 20, 30, 63

[16] Joel E Moore. The birth of topological insulators. *Nature*, 464(7286):194, 2010. 2, 13

[17] Hualing Zeng, Junfeng Dai, Wang Yao, Di Xiao, and Xiaodong Cui. Valley polarization in mos2 monolayers by optical pumping. *Nature nanotechnology*, 7(8):490, 2012. 2, 30

[18] Jianpeng Liu, Kasra Hejazi, and Leon Balents. Floquet engineering of multiorbital mott insulators: Applications to orthorhombic titanates. *Physical review letters*, 121(10):107201, 2018. 2

[19] YH Wang, Hadar Steinberg, Pablo Jarillo-Herrero, and Nuh Gedik. Observation of floquet-bloch states on the surface of a topological insulator. *Science*, 342(6157):453–457, 2013. 2, 15, 31

[20] Paul C. M. Planken, Han-Kwang Nienhuys, Huib J. Bakker, and Tom Wenckebach. Measurement and calculation of the orientation dependence of terahertz pulse detection in znte. *Journal of the Optical Society of America B*, 18(3):313–317, 2001. 2, 12, 56, 57

[21] Scott A Crooker, David D Awschalom, and Nitin Samarth. Time-resolved faraday rotation spectroscopy of spin dynamics in digital magnetic heterostructures. *IEEE Journal of selected topics in quantum electronics*, 1(4):1082–1092, 1995. 2

[22] Yun-Shik Lee. *Principles of terahertz science and technology*, volume 170. Springer Science & Business Media, 2009. 4, 6, 7, 8, 11, 12, 29, 48

[23] TR Globus, DL Woolard, T Khromova, TW Crowe, M Bykhovskaia, BL Gelmont, J Hesler, and AC Samuels. Thz-spectroscopy of biological molecules. *Journal of biological physics*, 29(2-3):89–100, 2003. 4

[24] Rupert Huber, Robert A Kaindl, Ben A Schmid, and Daniel S Chemla. Broadband terahertz study of excitonic resonances in the high-density regime in gaas/alxga1-xas quantum wells. *Physical Review B*, 72(16):161314, 2005. 4

[25] Martin Van Exter, Ch Fattinger, and D Grischkowsky. Terahertz time-domain spectroscopy of water vapor. *Optics letters*, 14(20):1128–1130, 1989. 5, 36, 55

[26] OV Kibis, K Dini, IV Iorsh, and IA Shelykh. All-optical band engineering of gapped dirac materials. *Physical Review B*, 95(12):125401, 2017. 5, 15, 16, 17

[27] Alvaro Gómez-León and Gloria Platero. Floquet-bloch theory and topology in periodically driven lattices. *Physical review letters*, 110(20):200403, 2013. 5, 31

[28] Fahad Mahmood, Ching-Kit Chan, Zhanybek Alpichshev, Dillon Gardner, Young Lee, Patrick A Lee, and Nuh Gedik. Selective scattering between floquet–bloch and volkov states in a topological insulator. *Nature Physics*, 12(4):306, 2016. 5

[29] Susan L Dexheimer. *Terahertz spectroscopy: principles and applications*. CRC press, 2007. 6, 7, 9, 10

[30] Robert W Boyd. *Nonlinear optics*. Elsevier, 2003. 6, 8, 10

[31] Ajay Nahata, Aniruddha S Weling, and Tony F Heinz. A wideband coherent terahertz spectroscopy system using optical rectification and electro-optic sampling. *Applied physics letters*, 69(16):2321–2323, 1996. 9, 48, 54

[32] J Hebling, AG Stepanov, G Almási, B Bartal, and J Kuhl. Tunable thz pulse generation by optical rectification of ultrashort laser pulses with tilted pulse fronts. *Applied Physics B*, 78(5):593–599, 2004. 9

[33] Pierre Delplace, Álvaro Gómez-León, and Gloria Platero. Merging of dirac points and floquet topological transitions in ac-driven graphene. *Physical Review B*, 88(24):245422, 2013. 13

[34] Yi Zhang, Tay-Rong Chang, Bo Zhou, Yong-Tao Cui, Hao Yan, Zhongkai Liu, Felix Schmitt, James Lee, Rob Moore, and Yulin Chen. Direct observation of the transition from indirect to direct bandgap in atomically thin epitaxial mose2. *Nature nanotechnology*, 9(2):111, 2014. 13

[35] Kin Fai Mak and Jie Shan. Photonics and optoelectronics of 2d semiconductor transition metal dichalcogenides. *Nature Photonics*, 10(4):216, 2016. 13

[36] Di Xiao, Gui-Bin Liu, Wanxiang Feng, Xiaodong Xu, and Wang Yao. Coupled spin and valley physics in monolayers of mos2 and other group-vi dichalcogenides. *Physical review letters*, 108(19):196802, 2012. 13

[37] Hernán L Calvo, Horacio M Pastawski, Stephan Roche, and Luis EF Foa Torres. Tuning laser-induced band gaps in graphene. *Applied Physics Letters*, 98(23):232103, 2011. 14

[38] Takashi Oka and Hideo Aoki. Photovoltaic hall effect in graphene. *Physical Review B*, 79(8):081406, 2009. PRB. 14, 15

[39] Takuya Kitagawa, Takashi Oka, Arne Brataas, Liang Fu, and Eugene Demler. Transport properties of nonequilibrium systems under the application of light: Photoinduced quantum hall insulators without landau levels. *Physical Review B*, 84(23):235108, 2011. 15

[40] FHM Faisal and JZ Kamiński. Floquet-bloch theory of high-harmonic generation in periodic structures. *Physical Review A*, 56(1):748, 1997. 15, 31

[41] Thibault Dartigalongue and François Hache. Precise alignment of a longitudinal pockels cell for time-resolved circular dichroism experiments. *JOSA B*, 20(8):1780–1787, 2003. 17, 40

[42] Stanford Research Systems. Manual, sr830 operation, 1993. 21, 51

[43] Charles A. Schmuttenmaer. Exploring dynamics in the far-infrared with terahertz spectroscopy. *Chemical Reviews*, 104(4):1759–1780, 2004. 23, 24

[44] Krzysztof Iwaszczuk, David G Cooke, Masazumi Fujiwara, Hideki Hashimoto, and Peter Uhd Jepsen. Simultaneous reference and differential waveform acquisition in time-resolved terahertz spectroscopy. *Optics Express*, 17(24):21969–21976, 2009. 25

[45] AA Makhnev, LV Nomerovannaya, TV Kuznetsova, OE Tereshchenko, and KA Kokh. Optical properties of bitei semiconductor with a strong rashba spin-orbit interaction. *Optics and Spectroscopy*, 117(5):764–768, 2014. 27

[46] J Reimann, CP Schmid, S Schlauderer, F Langer, C Lange, PG Hawkins, JT Steiner, U Huttner, SW Koch, and M Kira. Lightwave control of dirac electrons and the valley pseudospin. In *Nonlinear Optics*, page NF2A. 1. Optical Society of America. 27, 63

[47] Albert Feldman, William S Brower Jr, and Deane Horowitz. Optical activity and faraday rotation in bismuth oxide compounds. *Applied Physics Letters*, 16(5):201–202, 1970. 29

[48] J Karch, P Olbrich, M Schmalzbauer, C Zoth, C Brinsteiner, M Fehrenbacher, U Wurstbauer, MM Glazov, SA Tarasenko, and EL Ivchenko. Dynamic hall effect driven by circularly polarized light in a graphene layer. *Physical review letters*, 105(22):227402, 2010. 29, 63

[49] R Shimano, G Yumoto, JY Yoo, R Matsunaga, S Tanabe, H Hibino, T Morimoto, and H Aoki. Quantum faraday and kerr rotations in graphene. *Nature communications*, 4:1841, 2013. 29, 50, 63

[50] Jianming Dai, Jiangquan Zhang, Weili Zhang, and Daniel Grischkowsky. Terahertz time-domain spectroscopy characterization of the far-infrared absorption and index of refraction of high-resistivity, float-zone silicon. *JOSA B*, 21(7):1379–1386, 2004. 37

[51] Nardeep Kumar, Qiannan Cui, Frank Ceballos, Dawei He, Yongsheng Wang, and Hui Zhao. Exciton-exciton annihilation in mose2 monolayers. *Physical Review B*, 89(12):125427, 2014. 47, 63

[52] James W Lewis, Robert A Goldbeck, David S Kliger, Xiaoliang Xie, Robert C Dunn, and John D Simon. Time-resolved circular dichroism spectroscopy: experiment, theory, and applications to biological systems. *The Journal of Physical Chemistry*, 96(13):5243–5254, 1992. 47

[53] Hanju Rhee, Young-Gun June, Jang-Soo Lee, Kyung-Koo Lee, Jeong-Hyon Ha, Zee Hwan Kim, Seung-Joon Jeon, and Minhaeng Cho. Femtosecond characterization of vibrational optical activity of chiral molecules. *Nature*, 458(7236):310, 2009. 47

[54] Reiko Kuroda, Takunori Harada, and Yohji Shindo. A solid-state dedicated circular dichroism spectrophotometer: Development and application. *Review of Scientific Instruments*, 72(10):3802–3810, 2001. 47

[55] Thierry Buffeteau, François Lagugné-Labarthet, and Claude Sourisseau. Vibrational circular dichroism in general anisotropic thin solid films: measurement and theoretical approach. *Applied spectroscopy*, 59(6):732–745, 2005. 47

[56] Christoph K Hitzenberger, Erich Götzinger, Markus Sticker, Michael Pircher, and Adolf F Fercher. Measurement and imaging of birefringence and optic axis orientation by phase resolved polarization sensitive optical coherence tomography. *Optics express*, 9(13):780–790, 2001. 48, 50

[57] Wang-Kong Tse and Allan H MacDonald. Giant magneto-optical kerr effect and universal faraday effect in thin-film topological insulators. *Physical review letters*, 105(5):057401, 2010. 50

[58] GS Jenkins, DC Schmadel, and HD Drew. Simultaneous measurement of circular dichroism and faraday rotation at terahertz frequencies utilizing electric field sensitive detection via polarization modulation. *Review of Scientific Instruments*, 81(8):083903, 2010. 50

[59] Michael Oestreich, M Römer, Rolf J Haug, and D Hägele. Spin noise spectroscopy in gaas. *Physical review letters*, 95(21):216603, 2005. 50

[60] R Valdés Aguilar, AV Stier, W Liu, LS Bilbro, DK George, N Bansal, L Wu, J Cerne, AG Markelz, and Seongshik Oh. Terahertz response and colossal kerr rotation from the surface states of the topological insulator bi2se3. *Physical review letters*, 108(8):087403, 2012. 51

[61] A Rice, Y Jin, XF Ma, X-C Zhang, D Bliss, J Larkin, and M Alexander. Terahertz optical rectification from 110 zinc-blende crystals. *Applied physics letters*, 64(11):1324–1326, 1994. 56

[62] János Hebling, Ka-Lo Yeh, Matthias C Hoffmann, Balázs Bartal, and Keith A Nelson. Generation of high-power terahertz pulses by tilted-pulse-front excitation and their application possibilities. *JOSA B*, 25(7):B6–B19, 2008. 61

[63] Xingli Wang, Yongji Gong, Gang Shi, Wai Leong Chow, Kunttal Keyshar, Gonglan Ye, Robert Vajtai, Jun Lou, Zheng Liu, and Emilie Ringe. Chemical vapor deposition growth of crystalline monolayer mose2. *ACS nano*, 8(5):5125–5131, 2014. 62, 63

[64] Kostya S Novoselov, Andre K Geim, SVb Morozov, Da Jiang, Michail I Katsnelson, IVa Grigorieva, SVb Dubonos, Firsov, and AA. Two-dimensional gas of massless dirac fermions in graphene. *Nature*, 438(7065):197, 2005. 63

[65] Di Xiao, Wang Yao, and Qian Niu. Valley-contrasting physics in graphene: magnetic moment and topological transport. *Physical Review Letters*, 99(23):236809, 2007. 63